

# Impact of extreme spins and mass ratios on the post-merger observables of high-mass binary neutron stars

L. Jens Papenfort,<sup>1\*</sup> Elias R. Most,<sup>2,3,4</sup> Samuel Tootle<sup>1</sup> and Luciano Rezzolla<sup>1,5,6</sup>

<sup>1</sup>*Institut für Theoretische Physik, Goethe Universität, Max-von-Laue-Str. 1, 60438 Frankfurt am Main, Germany*

<sup>2</sup>*Princeton Center for Theoretical Science, Princeton University, Princeton, NJ 08544, USA*

<sup>3</sup>*Princeton Gravity Initiative, Princeton University, Princeton, NJ 08544, USA*

<sup>4</sup>*School of Natural Sciences, Institute for Advanced Study, Princeton, NJ 08540, USA*

<sup>5</sup>*School of Mathematics, Trinity College, Dublin 2, Ireland*

<sup>6</sup>*Frankfurt Institute for Advanced Studies, Ruth-Moufang-Str. 1, 60438 Frankfurt am Main, Germany*

Accepted XXX. Received YYY; in original form ZZZ

## ABSTRACT

The gravitational-wave events GW170817 and GW190425 have led to a number of important insights on the equation of state of dense matter and the properties of neutron stars, such as their radii and the maximum mass. Some of these conclusions have been drawn on the basis of numerical-relativity simulations of binary neutron-star mergers with vanishing initial spins. While this may be a reasonable assumption in equal-mass systems, it may be violated in the presence of large mass asymmetries accompanied by the presence of high spins. To quantify the impact of high spins on multi-messenger gravitational-wave events, we have carried out a series of high-mass binary neutron-star mergers with a highly spinning primary star and large mass asymmetries that have been modelled self-consistently using two temperature-dependent equations of state. We show that, when compared with equal-mass, irrotational binaries, these systems can lead to significant differences in the remnant lifetime, in the dynamical ejecta, in the remnant disc masses, in the secular ejecta, and on the bulk kilonova properties. These differences could be exploited to remove the degeneracy between low- and high-spin priors in the detection of gravitational waves from binary neutron-star mergers.

**Key words:** gravitational waves — stars: neutron — binary neutron-star mergers

## 1 INTRODUCTION

The first gravitational-wave (GW) detection of binary neutron-star (BNS) mergers by means of the events GW170817 (The LIGO Scientific Collaboration & The Virgo Collaboration 2017) GW190425 (Abbott et al. 2020) and the potential black hole neutron star (BHNS) binary GW190814 (The LIGO Scientific Collaboration et al. 2020), have led to a multitude of conclusions on the nature of the most extremely compact states of matter. Especially GW170817, thanks to its electromagnetic counterpart, has enabled us to put constraints on the equation of state (EOS) of nuclear matter (see e.g., Margalit & Metzger 2017; Bauswein et al. 2017; Rezzolla et al. 2018; Ruiz et al. 2018; Annala et al. 2018; Radice et al. 2018a; Most et al. 2018; De et al. 2018; Abbott et al. 2018; Montaña et al. 2019; Raithel et al. 2018; Tews et al. 2018; Malik et al. 2018; Koeppel et al. 2019; Shibata et al. 2019; Nathanael et al. 2021). The assumption that the remnant collapsed to a black hole has resulted in an upper bound on the maximum mass of a neutron star (NS) of  $M_{\text{TOV}} \lesssim 2.3 M_{\odot}$  when applying conservative assumptions on the merger remnant and its properties (see e.g., Margalit & Metzger 2017; Rezzolla et al. 2018; Ruiz et al. 2018; Shibata et al. 2019; Nathanael et al. 2021). While the total mass of GW170817 was presumably not large enough for a

prompt collapse to a black hole (BH) at merger, this is likely to be the case for GW190425. Given the degeneracy between effects on the inspiral waveform induced by the tidal deformations and the spins (Hannam et al. 2014; Favata 2014; Agathos et al. 2015; Harry & Hinderer 2018; Zhu et al. 2018), the mass ratio between the constituents of GW170817 and GW190425 is not well constrained, leading to values of  $1 \leq q^{-1} \lesssim 2.5$  depending on whether low- or high-spin priors are applied (Abbott et al. 2019, 2020, see also Most et al. (2020a)). It should be noted that the spin distributions in the case of low-spin priors are compatible with a spin that is essentially zero and provide a tighter constraint on the mass ratio, while the high-spin priors include extreme rotational states and yield a larger uncertainty in the mass ratio. In particular, it has been shown that, if the secondary of the GW190814 event was once a highly spinning NS, it would lead to a potential rotation frequency of  $f = \Omega/2\pi$  of 1.21 (1.14) kHz with  $\chi_2 = 0.49$ , using a typical NS radius of  $R = 12.5$  (13) km (Most et al. 2020b).

At the same time, pulsar observations have led to a rich catalogue of observable NSs through independent electromagnetic channels (Manchester et al. 2005; Lorimer 2008; Lynch et al. 2012; Benacquista & Downing 2013; Alsing et al. 2018; Tauris et al. 2017; Ridolfi et al. 2021), including observational lower limits on  $M_{\text{TOV}}$  (Demorest et al. 2010; Antoniadis et al. 2013; Fonseca et al. 2016; Arzoumanian et al. 2018; Cromartie et al. 2020), the evidence for extreme rotational

\* E-mail: papenfort@th.physik.uni-frankfurt.de

frequencies (Hessels et al. 2006), as well as binary-pulsar systems with significant mass asymmetries (Martinez et al. 2015; Lazarus et al. 2016; Tauris & Janka 2019), companions with appreciable spin frequencies (Lyne et al. 2004; Stovall et al. 2018), and masses in X-ray binaries as low as  $\approx 1.1 M_{\odot}$  (Rawls et al. 2011). Based on these observational evidences, we hereafter assume a conservative mass range for the mass of a nonrotating NS to be  $1.1 \lesssim M_{\text{NS}} \lesssim 2.3$  for NSs in BNS systems. In addition, the increasingly sophisticated parametric studies on population synthesis and analyses of possible (sub-)population binary-formation channels (see e.g., Dominik et al. 2013; Tauris et al. 2017; Kruckow et al. 2018; Andrews & Mandel 2019), suggest that the ratio in masses in a BNS system should lie in the range  $0.5 \lesssim q \lesssim 1.0$ .

On the other hand, the range of spins in BNS systems is far less constrained. The highly spinning millisecond pulsars known today are most probably all recycled pulsars which gained angular momentum through different accretion processes in binaries involving a donor star (Burderi et al. 1999; Tauris et al. 2012; Miller & Miller 2015; Tauris et al. 2015; Tauris et al. 2017), where the most mass is accreted in common-envelope evolutions. Theoretical estimations of the amount of spin-up by mass accretion processes show that significant mass fractions have to be accreted to reach the sub-millisecond scale (Burderi et al. 1999; Tauris et al. 2012), while simulations of the common-envelope phase suggest a limit of  $M_{\text{acc}} \lesssim 0.1 M_{\odot}$  (MacLeod & Ramirez-Ruiz 2015; Cruz-Osorio & Rezzolla 2020) with limited efficiency of angular momentum transport (Murguía-Berthier et al. 2017). Nonetheless, there is evidence of systems potentially accreting with rates far beyond the Eddington limit (Israel et al. 2017), while the magnetic field should be damped quickly and thus the star would not be visible as a pulsar on longer time-scales.

Over the past two decades, a large number of theoretical studies have been carried out to understand the effects of mass asymmetry in BNS mergers, mostly considering rather small asymmetries, i.e.,  $q \gtrsim 0.7$  with irrotational NS constituents (see, e.g., Shibata et al. 2003; Rezzolla et al. 2010; Bauswein et al. 2013; Neilsen et al. 2014; Dietrich et al. 2015; Radice et al. 2016b; Dietrich et al. 2017a; Radice et al. 2018a; Papenfort et al. 2018; Most & Raithe 2021). Smaller mass ratios, e.g.,  $q \lesssim 0.5$ , have been simulated only with a piecewise polytropic EOS which was either stiff (Dietrich et al. 2015, 2017a), or rather soft (Tichy et al. 2019). These studies have then been followed by the first evolutions of BNS systems with  $q \approx 0.45$  adopting tabulated temperature and electron-fraction dependent EOSs (Most et al. 2021; Papenfort et al. 2020). In summary, this large bulk of work points out that a stronger mass asymmetry leads to a more violent tidal disruption of the secondary, which is accompanied by an increase of the dynamical ejecta through tidal tails at lower electron fraction, while the systems retain a larger disc mass after the collapse of the remnant as already pointed out by Shibata & Taniguchi (2006) and Rezzolla et al. (2010).

Additionally, attention has also been paid to investigation of binaries with various degrees of spin prior to the merger (Kastaun et al. 2013; Bernuzzi et al. 2014; East et al. 2016b; Dietrich et al. 2017b; East et al. 2019; Most et al. 2019c, 2021). These works have pointed out that a significant amount of stellar spin aligned with orbital angular momentum can increase the lifetime of the merger remnant and leave an imprint on the final spin of the BH produced when the remnant collapses, attaining an upper limit of  $J/M^2 \approx 0.89$  the dimensionless spin (Kastaun et al. 2013; Bernuzzi et al. 2014). Interestingly, the combination of high spins of up to  $|\chi_{1,2}| = 0.756$  and highly eccentric orbits can also increase the lifetime of the remnant (East et al. 2016b), while large aligned spins alone can boost the development of a one-arm instability in the remnants and in-

crease the disc masses (East et al. 2019). At the same time, the comparison of moderate spins with  $|\chi_{1,2}| = 0.1$  in binaries with mass asymmetry in the range  $q \in [0.66, 1]$ , has shown that these are subdominant to the effects of mass asymmetry (Dietrich et al. 2017b). More recently, BNS configurations with strongly spinning and equal-mass constituents having (anti-)aligned spins and fully temperature-dependent EOSs have been shown to exhibit a strong suppression of the dynamical ejecta for aligned spins (Most et al. 2019c). In addition, it has been shown how highly asymmetric binaries with  $q = 0.5$  and significant spin of the massive primary (whose mass is close to the maximum mass for either rotating or nonrotating models), can produce dynamical ejecta with a significant fast component that can be used to discriminate this BNS from a BH-NS binary (Most et al. 2021).

At the same time, considerable effort has been put into constraining the the threshold mass to prompt collapse at merger,  $M_{\text{th}}$ , that is, the critical mass above which the merged object collapses on a dynamical timescale (Bauswein et al. 2013; Koepfel et al. 2019; Agathos et al. 2020; Bauswein et al. 2020; Tootle et al. 2021; Perego et al. 2021; Kölsch et al. 2021). The prompt collapse scenario provides important constraints on follow-up electromagnetic radiation since it affects the amount of unbound matter in the system, with the latter being useful to constrain the survival time of the remnant (Gill et al. 2019). It was realised early that the threshold mass can be parametrized at least approximately in terms of the mass of the binary and hence of the maximum mass  $M_{\text{TOV}}$  (Shibata et al. 2005; Baiotti et al. 2008; Bauswein et al. 2013), such that  $M_{\text{th}} \propto M_{\text{TOV}}$ . More recent studies have explored this process including more realistic, temperature-dependent EOSs (Koepfel et al. 2019; Agathos et al. 2020; Bauswein et al. 2020), incorporating the effects of mass asymmetry (Bauswein et al. 2021) and non-negligible spin in the binary (Tootle et al. 2021). Overall, these studies have shown that smaller mass ratios reduce the threshold mass and increase both the dynamically ejected mass and the mass in the disc mass around the promptly formed BH. At the same time, the inclusion of spin reveals that  $M_{\text{th}}$  can increase (decrease) by 5% (10%) for binaries that have spins aligned (antialigned) with the orbital angular momentum and that the threshold mass has a non-monotonic dependence on the mass asymmetry in the system (Tootle et al. 2021).

We here provide the first systematic study on BNS configurations significantly above the irrotational threshold mass in conjunction with a highly spinning primary companion in a binary with strong mass asymmetries. We point out important differences between the stability of the merger remnant, its post-merger properties, the resulting ejecta, and the disc masses after collapse, when extreme spins are considered. We do this after employing two tabulated temperature- and electron-fraction dependent EOSs and a neutrino leakage scheme. Overall, we find that the inclusion of extreme spin rates can provide significant differences in the threshold mass, dynamical ejecta, remnant disc masses and therefore in the amount of secular ejecta. In turn, these differences could be used to discriminate between low- and high-spin priors in the detection of GWs from BNS mergers with such high masses.

The plan of the paper is as follows. In Sec. 2 we present our numerical setup, while in Sec. 3 we illustrate the dynamics from the various models considered, contrasting the similarities and the differences, and collecting the most salient features. Finally, Sec. 4 provides a concluding discussion and the prospects of future work.

binary model	EOS	$M_1$ [ $M_\odot$ ]	$M_2$ [ $M_\odot$ ]	$M_{b,1}$ [ $M_\odot$ ]	$M_{b,2}$ [ $M_\odot$ ]	$M_\infty$ [ $M_{\text{th}}^{1,0}$ ]	$M_\infty$ [ $M_\odot$ ]	$M_{\text{ADM}}$ [ $M_\odot$ ]	$q$	$\tilde{\chi}_{\text{init}}$	$\chi_1$	$\chi_{\text{eff}}$	$M_{\text{disc}}$ [ $M_\odot$ ]	$\tau_c$ [ms]	lifetime symbol
TNT-10.5-0.30-0.837	TNTYST	1.741	1.458	2.155	1.983	1.105	3.199	3.166	0.837	0.944	0.30	0.158	0.009	0.7	▽
TNT-10.5-0.30-1.000	TNTYST	1.600	1.600	1.799	1.809	1.105	3.199	3.166	1.000	0.939	0.30	0.150	0.019	0.6	▽
TNT-10.5-0.45-0.675	TNTYST	1.910	1.289	2.192	1.418	1.105	3.199	3.167	0.675	0.978	0.45	0.268	0.152	2.4	▽
TNT-10.5-0.45-0.837	TNTYST	1.741	1.458	1.969	1.628	1.105	3.199	3.166	0.837	0.981	0.45	0.244	0.029	1.0	▽
TNT-10.5-0.45-1.000	TNTYST	1.600	1.600	1.788	1.809	1.105	3.199	3.166	1.000	0.970	0.45	0.225	0.092	0.7	▽
TNT-10.5-0.60-0.675	TNTYST	1.910	1.289	2.166	1.418	1.105	3.199	3.168	0.675	1.023	0.60	0.358	0.227	> 36.4	△
TNT-10.5-0.60-0.837	TNTYST	1.741	1.458	1.949	1.628	1.105	3.199	3.166	0.837	1.018	0.60	0.326	0.118	5.7	□
TNT-10.5-0.60-1.000	TNTYST	1.600	1.600	1.772	1.809	1.105	3.199	3.165	1.000	1.001	0.60	0.300	0.176	1.2	▽
TNT-05.0-0.45-0.600	TNTYST	1.899	1.139	2.176	1.237	1.050	3.039	3.010	0.600	1.034	0.45	0.281	0.240	> 34.2	△
TNT-05.0-0.45-0.800	TNTYST	1.688	1.350	1.899	1.492	1.050	3.039	3.006	0.800	1.048	0.45	0.250	0.088	9.9	□
TNT-05.0-0.45-1.000	TNTYST	1.519	1.519	1.686	1.704	1.050	3.039	3.006	1.000	1.036	0.45	0.225	0.100	6.0	□
TNT-05.0-0.60-0.600	TNTYST	1.899	1.139	2.151	1.237	1.050	3.039	3.010	0.600	1.086	0.60	0.375	0.262	> 34.8	△
TNT-05.0-0.60-0.800	TNTYST	1.688	1.350	1.883	1.492	1.050	3.039	3.007	0.800	1.089	0.60	0.333	0.137	> 35.9	△
TNT-05.0-0.60-1.000	TNTYST	1.519	1.519	1.674	1.704	1.050	3.039	3.007	1.000	1.068	0.60	0.300	0.231	> 36.2	△
BHB-10.8-0.30-0.837	BHBΛΦ	1.904	1.595	2.155	1.771	1.109	3.500	3.460	0.837	0.919	0.30	0.163	0.034	0.7	▽
BHB-10.8-0.45-0.675	BHBΛΦ	2.089	1.410	2.381	1.544	1.109	3.500	3.461	0.675	0.954	0.45	0.268	0.187	0.7	▽
BHB-10.8-0.45-0.837	BHBΛΦ	1.904	1.595	2.140	1.771	1.109	3.500	3.460	0.837	0.956	0.45	0.244	0.065	0.8	▽
BHB-10.8-0.60-0.675	BHBΛΦ	2.089	1.410	2.355	1.544	1.109	3.500	3.461	0.675	0.998	0.60	0.358	0.259	2.4	▽
BHB-10.8-0.60-0.837	BHBΛΦ	1.904	1.595	2.121	1.771	1.109	3.500	3.460	0.837	0.992	0.60	0.326	0.162	0.9	▽
BHB-05.0-0.60-0.600	BHBΛΦ	2.071	1.242	2.331	1.343	1.050	3.314	3.279	0.600	1.065	0.60	0.375	0.289	8.4	□
BHB-05.0-0.60-0.800	BHBΛΦ	1.841	1.472	2.042	1.619	1.050	3.314	3.277	0.800	1.066	0.60	0.333	0.158	> 39.1	△
BHB-05.0-0.60-1.000	BHBΛΦ	1.657	1.657	1.817	1.848	1.050	3.314	3.277	1.000	1.045	0.60	0.300	0.191	0.9	▽
BHB-02.5-0.45-0.600	BHBΛΦ	2.022	1.213	2.292	1.308	1.025	3.235	3.202	0.600	1.044	0.45	0.281	0.262	1.5	▽
BHB-02.5-0.45-0.800	BHBΛΦ	1.797	1.437	2.004	1.576	1.025	3.235	3.199	0.800	1.057	0.45	0.250	0.146	25.2	△
BHB-02.5-0.45-1.000	BHBΛΦ	1.617	1.617	1.781	1.798	1.025	3.235	3.199	1.000	1.044	0.45	0.225	0.128	2.9	▽
BHB-02.5-0.60-0.600	BHBΛΦ	2.022	1.213	2.268	1.308	1.025	3.235	3.202	0.600	1.097	0.60	0.375	0.307	26.5	△
BHB-02.5-0.60-0.800	BHBΛΦ	1.797	1.437	1.988	1.576	1.025	3.235	3.199	0.800	1.098	0.60	0.333	0.153	> 38.8	△
BHB-02.5-0.60-1.000	BHBΛΦ	1.617	1.617	1.770	1.798	1.025	3.235	3.199	1.000	1.077	0.60	0.300	0.246	1.3	▽

**Table 1.** Summary of the binary configurations considered. The different columns list: the binary model, the EOS, the gravitational masses  $M_{1,2}$  of both stars in isolation, the baryonic masses  $M_{b,1,2}$ , the ratio between the total gravitational mass at infinite separation  $M_\infty$  and the irrotational threshold mass of the given EOS  $M_{\text{th}}^{1,0}$ , the ADM mass of the initial data  $M_{\text{ADM}}$ , the initial rescaled total dimensionless angular momentum  $\tilde{\chi}_{\text{init}}$  (see Eq. (1)), the mass ratio  $q := M_2/M_1 \leq 1$ , the dimensionless spin angular momentum of the primary star  $\chi_1$ , the resulting effective spin of the system  $\chi_{\text{eff}}$ , the post-merger remnant disc mass  $M_{\text{disc}}$ , the survival time of the remnant after merger  $\tau_c$ , and a symbol indicating the remnant lifetime. In particular, a short-lived remnant is marked by ▽, a medium-lived remnant by □ and a long-lived remnant by △ (see Sec. 3.2 for a definition). The secondary is assumed to be irrotational in all cases, i.e.,  $\chi_2 = 0$  and  $M_\infty$  is fixed to be larger than the corresponding threshold mass  $M_{\text{th}}^{1,0}$  of the given EOS (see Table 2).

EOS	$M_{\text{TOV}}$ [ $M_\odot$ ]	$R_{1.4}$ [km]	$C_{1.4}$	$M_{\text{th}}^{1,0}$ [ $M_{\text{TOV}}$ ]	$M_{\text{th}}^{1,0}$ [ $M_\odot$ ]
TNTYST+	2.23	11.54	0.28	1.298	2.894
BHBΛΦ	2.10	13.22	0.23	1.503	3.156

**Table 2.** Properties of the tabulated nuclear EOSs utilised in this study: the softer TNTYST (Togashi et al. 2017) and the stiffer BHBΛΦ (Banik et al. 2014). We report the maximum mass of a nonrotating NS,  $M_{\text{TOV}}$ , together with the radius at a mass of  $1.4 M_\odot$ ,  $R_{1.4}$ , and the corresponding compactness,  $C_{1.4} := 1.4/R_{1.4}$ . Also shown are the threshold masses as reported by Koepfel et al. (2019) for an equal-mass irrotational BNS,  $M_{\text{th}}^{1,0}$ .

## 2 METHODS

The equations of relativistic hydrodynamics in dynamical spacetimes are solved by the Frankfurt/IllinoisGRMHD code (FIL) (Most et al. 2019b,a) derived from the IllinoisGRMHD code (Etienne et al. 2015), and is built on top of the Einstein Toolkit (Loeffler et al. 2012). It implements high-order (fourth) conservative finite-difference methods (Del Zanna et al. 2007) for the fluid and magnetic field evolution, supports temperature and electron-fraction

dependent EOSs, and neutrino cooling and weak interactions by a neutrino leakage scheme (Ruffert et al. 1996; Rosswog & Liebendörfer 2003; Galeazzi et al. 2013). The properties of nuclear matter are modeled using the TNTYST (Togashi et al. 2017) and BHBΛΦ (Banik et al. 2014) EOS. The latter is based on the DD2 EOS (Hempel & Schaffner-Bielich 2010) but incorporates hyperons (Banik et al. 2014) at high densities. Characteristic properties of both EOS can be found in Tab. 2, with BHBΛΦ being stiffer and leading to larger radii of the stars. Besides, these EOS cover a range of maximum masses and radii consistent with GW170817.

The code also implements a constraint-damping formulation of the Z4 form of the Einstein field equations (Bona et al. 2003; Bernuzzi & Hilditch 2010; Alic et al. 2012). We model the initial binary configurations via the solution of the constraint equations solved using the extended conformal thin-sandwich (XCTS) formalism (Pfeiffer & York 2003; Pfeiffer & York 2005). The highly spinning companion is constructed following the formalism proposed by Tichy (2012), for which the velocity field of the star is a combination of an irrotational and of a uniformly rotating part (Tacik et al. 2015; Tsokaros et al. 2015, 2016; Papenfort et al. 2020). This is implemented using the

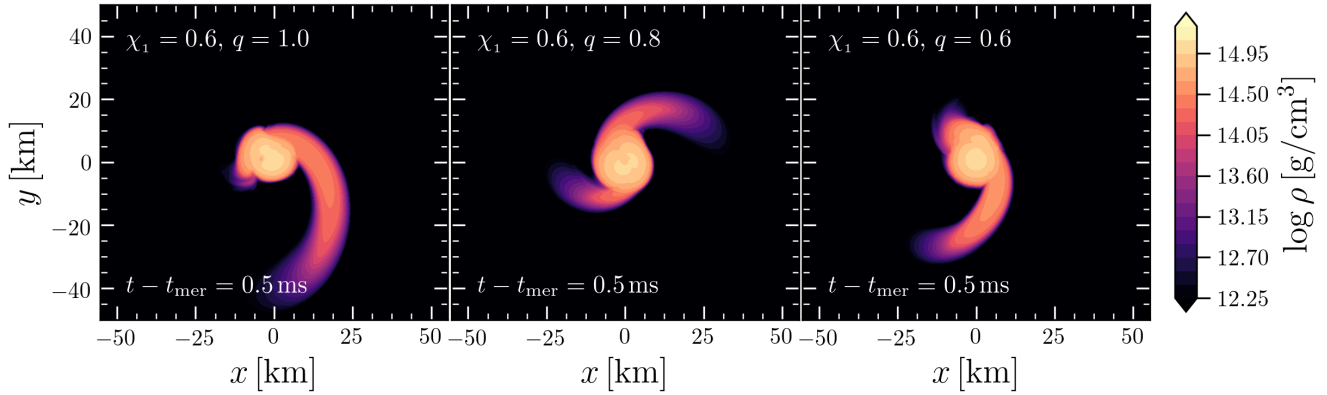


**Figure 1.** Rest-mass density distribution  $\rho$  on the equatorial plane of three representative simulations shortly after the merger, i.e.,  $t - t_{\text{mer}} = 0.5$  ms. The three binaries have  $\chi_1 = 0.6$  and mass ratios  $q \in \{1.0, 0.8, 0.6\}$  for the TNTYST at  $M_\infty/M_{\text{th}}^{1,0} = 1.05$ . At mass symmetry (*left*), the highly spinning primary is tidally disrupted, while at strong mass asymmetry (*right*) it is the irrotational secondary that is disrupted instead. At this spin magnitude, the intermediate mass ratio  $q = 0.8$  (*middle*) shows merger dynamics closer to a typical irrotational merger.

FUKA<sup>1</sup> code (Papenfort et al. 2020), which extends to general compact binary initial data the Kadath spectral library (Grandclement 2010). Note that although FIL solves the equations of general-relativistic magnetohydrodynamics, for simplicity, we set the magnetic field to zero in our analysis.

The computational domain is managed by the adaptive mesh-refinement driver Carpet (Schnetter et al. 2004) and features a set of nested Cartesian box-in-box levels. We have here used total of eight levels of refinement, with the finest one having a resolution of  $h = 0.16 M_\odot \approx 236$  m and with outermost box extending up to  $\approx 6000$  km. The resolution employed is rather high and sufficient to capture accurately the NSs, whose size depends on the mass ratio and on the spin rate (stars rotating near the mass shedding acquire a rather flattened shape). We note that we have conducted all of the simulations also at a lower resolution of  $h = 0.2 M_\odot \approx 295$  m and – in some cases – with a higher resolution of  $h = 0.133 M_\odot \approx 197$  m. The uncertainties that can be measured through this comparative analysis indicate that the errors are of a few tens of a percent at most. A more extended discussion detailing the various uncertainties in the different quantities can be found in the Appendix A.

Using as a reference the threshold mass for an equal-mass irrotational system as predicted by the quasi-universal relation of Koeppel et al. (2019), hereafter simply  $M_{\text{th}}^{1,0}$ , we have explored BNSs where the binary has masses up to  $\approx 1.1 M_{\text{th}}^{1,0}$  and the mass ratio can be as small as  $q = 0.6^2$ . This rather extreme systems can be constructed because the primary is very highly spinning, with a dimensionless spin in the range  $\chi_1 := J_{\text{ADM},1}/M_{\text{ADM},1}^2 \in \{0.30, 0.45, 0.60\}$ , where  $J_{\text{ADM},1}$  and  $M_{\text{ADM},1}$  are the ADM angular momentum and mass of the primary in isolation, respectively. In all cases, the spin axis is aligned with the orbital angular momentum, mostly for convenience rather than for realism. While placing all of the spin in the system in the primary is not only a convenient choice, it is in all likelihood also the most realistic one. Indeed, the astrophysical scenario reproduced

with our initial data corresponds, from an evolutionary point of view, to the case in which the primary NS has gained the additional spin angular momentum through mass transfer from the progenitor star of the secondary NS (see e.g., Tauris et al. 2017). In this scenario, therefore, the secondary has a spin which is much smaller than the primary and can effectively be treated as irrotational; a partially more extended investigation of the space of parameters to include less extreme spin magnitudes has already been presented by Tootle et al. (2021) and will part of our future work. Finally, all binaries start with an initial separation of 45 km and their initial properties are given in Tab. 1.

### 3 RESULTS

In this section we present the results of our numerical evolutions and discuss the effects introduced by the large amounts of spin in the primary star.

In total, we conducted 14 simulations for each EOS, with a total of 28 simulations. These consist of two sets for the TNTYST EOS and three for the BHB $\Lambda\Phi$  EOS. In each set, we select a binary after fixing the ADM mass of the system at infinite separation,  $M_\infty$ , in terms of the threshold mass for an equal-mass irrotational binary as found by Koeppel et al. (2019) for these EOSs; this quantity can be taken as a measure of the “mass criticality” in the system. More specifically, we consider binaries with ADM mass  $M_\infty/M_{\text{th}}^{1,0} \in \{1.050, 1.105\}$  for TNTYST and  $M_\infty/M_{\text{th}}^{1,0} \in \{1.025, 1.050, 1.109\}$  for BHB $\Lambda\Phi$ . Furthermore, for each binary we vary the mass asymmetry  $q$  between the two stars with  $q \in [0.6, 1.0]$ , but also the amount of spin of the primary,  $\chi_1$ , with  $\chi_1 \in [0.3, 0.6]$ . In this way, we can construct a table of 28 different configurations whose properties can be found in Tab. 1.

In the following subsections we present the results concerning the merger and post-merger dynamics, the stability of the remnant, as well as the dynamical mass ejection, the remnant disc masses, which are important for the secular ejecta and their implications on the resulting kilonova emission.

<sup>1</sup> <https://kadath.obspm.fr/fuka/>

<sup>2</sup> For simplicity, we have here employed a rescaling in terms of threshold mass for an equal-mass irrotational binary  $M_{\text{th}}^{1,0}$ , thus ignoring the corrections that are introduced by spin and mass ratio and presented by Tootle et al. (2021). While these are interesting, they do not provide additional information on the systematic behaviour.

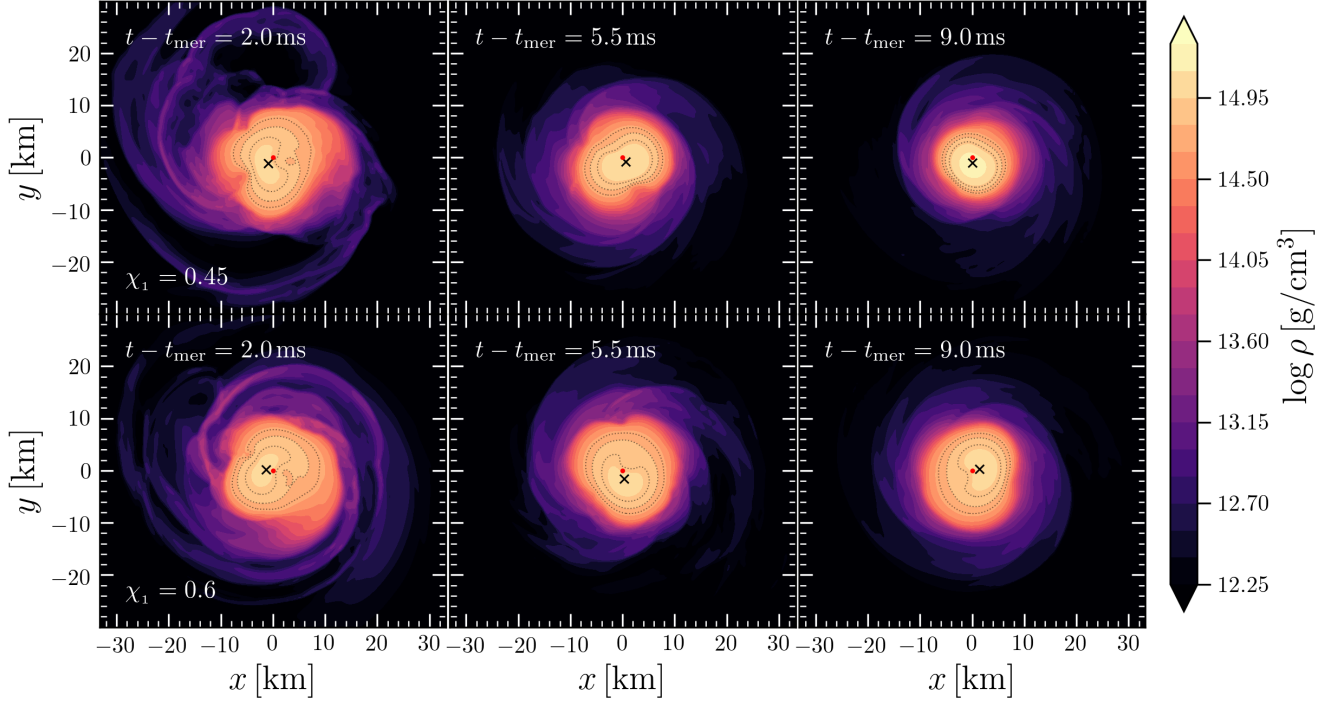


**Figure 2.** Rest-mass density distribution  $\rho$  on the equatorial plane of the two models TNT-05.0-0.45-0.800 and TNT-05.0-0.60-0.800 at different times in the early post-merger phase. Both systems exhibit a total mass which is 5% above  $M_{\text{th}}^{1.0}$  of the TNTYST EOS (see Tab. 1) with a dimensionless spin of the primary companion of  $\chi_1 = 0.45$  (top) and  $\chi_1 = 0.6$  (bottom), respectively. The black cross denotes the point of highest rest-mass density and the red dot marks the origin of the coordinates, representing the approximate location of the axis of rotation. In addition, three dotted contours at  $\log \rho \in \{14.7, 14.8, 14.9\}$  highlight the asymmetries of the matter distribution.

### 3.1 Merger and post-merger dynamics

As is well-known already from post-Newtonian dynamics, binary systems with highly spinning constituents experience longer inspirals with increasing spin of the primary due to the spin-orbit coupling and the net increased angular momentum, thus exhibiting different times of merger (Bernuzzi et al. 2014; Dietrich et al. 2015, 2017b; Most et al. 2019c). While this is interesting in its own right and important when constructing high-precision waveforms, hereafter we will concentrate on the violent merger process at these high masses, spins, and mass asymmetry.

As a representative set of models, we show in Fig. 1 snapshots of the rest-mass density at  $t - t_{\text{mer}} = 0.5$  ms after the merger of three models at different mass ratios and with the highest primary spin  $\chi_1 = 0.6$  for the TNTYST EOS. For all of them the total mass is 5% above the irrotational threshold mass, i.e.,  $M_{\infty}/M_{\text{th}}^{1.0} = 1.05$ .

At these high spins, there is an interesting transition in the star that is first disrupted tidally. More specifically, in the  $q = 1$  equal-mass case (left panel in Fig. 1), the disruption is suffered by the primary, which is also the only star carrying angular momentum. However, when a large asymmetry in the mass is present, as for the  $q = 0.6$  case (right panel in Fig. 1), then the disruption is suffered by the secondary, which is less massive and irrotational. In the intermediate case of  $q = 0.8$  (middle panel in Fig. 1), on the other hand, the disruption follows a pattern already encountered in the case of irrotational unequal-mass binaries. More specifically, the secondary appears to be disrupted first and accretes mass and angular momentum on the primary, that is also disrupted as a consequence. A more detailed investigation of this scenario, possibly including tracer particles (Bovard & Rezzolla

2017), will help determine with more precision the fate of the two star in this mass ratio, see also Most et al. (2021) for a similar scenario.

For binaries with the same spin magnitude but with larger mass criticality, i.e.,  $M_{\infty}/M_{\text{th}}^{1.0} = 1.105$ , the primary is less affected at merger in the case of  $q = 1$  and the tidal disruption much more contained. This trend becomes even stronger for equal-mass binaries with smaller primary spins, i.e.,  $\chi_1 = 0.45$ , where the dynamics is very similar to that of irrotational binaries. Nonetheless, the spin still has a noticeable impact at merger, especially in the  $q = 0.6$  cases, where the secondary is still disrupted strongly.

A qualitatively similar behaviour to the one discussed above for the TNTYST EOS applies also for the stiffer BHBAΦ EOS, although all of the dynamics is somewhat milder and the disruptions weaker already at a mass criticality of  $M_{\infty}/M_{\text{th}}^{1.0} = 1.05$ . This points out that the stellar compactness, and hence the EOS, also plays an important role in the subtle balance that is introduced near the merger between tidal forces (controlled by the mass ratio), centrifugal forces (controlled by the primary spin), and the overall strength of the gravitational potential (controlled by the total mass of the system). The most robust dynamical features of this picture can therefore be summarised as follows. First, in the equal-mass case the disruption is suffered by the highly spinning primary, as spin effects dominate in this case. Second, in the strongly mass asymmetric case, the disruption is instead suffered by the secondary, as tidal effects dominate in this case. Finally, in all cases, the tidal tails from the highly spinning primary carry large amounts of angular momentum, expanding quicker, potentially shocking partly into the tidal tail of the secondary.

Further into the post-merger phase, the merger remnants feature various degrees of asymmetry in the matter distribution, especially

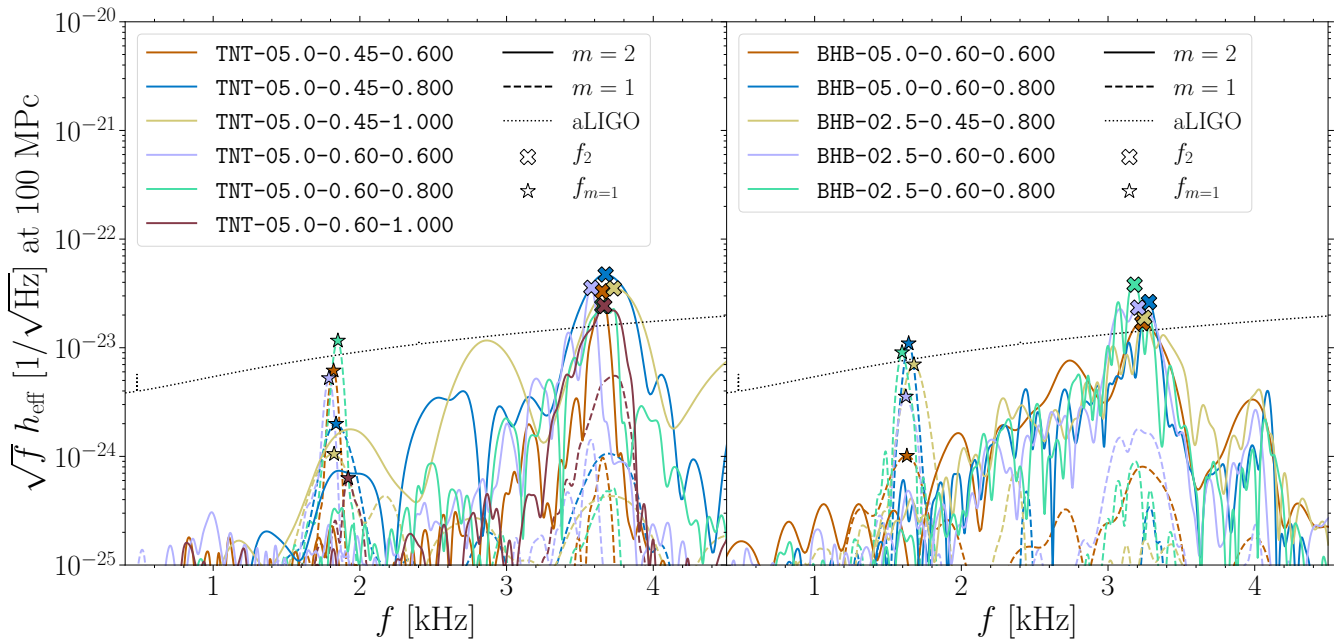


**Figure 3.** *Left panel:* GW-strain spectral density for a number of binaries with either the TNTYST (*left*) EOS. The spectra are computed over the time window between the merger and the collapse or till the end of the simulation; hence, they are different for different binaries. Marked with symbols are the positions of the dominant post-merger  $f_2$  and of the one-arm instability  $f_{m=1}$  frequencies, which are produced by  $(\ell = 2, m = 2)$  and  $(2, 1)$  deformations, respectively; shown with a dotted line is the sensitivity curve of Advanced LIGO. *Right panel:* The same as in the left panel but for the BHBA $\Phi$  EOS.

in the equatorial plane. Some representative examples are shown in Fig. 2 for two binaries with the TNTYST EOS being equally above the threshold mass (5%) and having the same mass ratio ( $q = 0.8$ ), but differing in the spin magnitude of the primary. Note how the asymmetry of the matter distribution is quite significant and is actually larger in the binary with the largest spin, i.e.,  $\chi_1 = 0.6$ . In both cases, a strong one-arm instability (or  $m = 1$ ) develops in the remnant (Bernuzzi et al. 2014; Paschalidis et al. 2015; East et al. 2016b,a; Lehner et al. 2016b; Radice et al. 2016a; East et al. 2019), and survives for significant amounts of time, providing potentially measurable imprints in the GW emission and disc winds (Nedora et al. 2019).

We next discuss the dynamics of the binaries examined in terms of their GW emission. While the inspiral leads to different merger times and to a different frequency evolution depending on the total mass, mass ratio, spin magnitude of the primary, and the tidal deformability, we focus on the post-merger remnant evolution. Of course, our discussion will necessarily exclude those binaries that are not at least short-lived (see Sec. 3.2 for some definitions).

To this scope, the spectrum of the post-merger GW emission for the TNTYST EOS (left panel) and for the BHBA $\Phi$  EOS are shown in Fig. 3, displaying the frequencies of the  $(\ell = 2, m = 2)$ -mode, together with the frequencies of the  $(2, 1)$ -mode. The spectrum of both modes is computed for the effective strain over a window starting at merger until the system undergoes a collapse or until the end of the simulation, in case of the models with a sufficiently long post-merger HMNS phase (see e.g. Takami et al. 2014; Papenfort et al. 2018, for details). The windowing is done by a Hann window to minimise spectral leakage from truncating the signal. The resulting spectra are further smoothed by a spline interpolation for presentation. The spectra show a clear contribution from the  $(2, 1)$ -mode with an expected frequency at  $f_{m=1} \approx 0.5 f_2$  – not to be confused with the  $f_1$  mode in the classification of Takami et al. (2014) – where  $f_2$  is the dominating  $(2, 2)$ -mode post-merger frequency (Bauswein & Janka

2012; Takami et al. 2014; Bernuzzi et al. 2015; Palenzuela et al. 2015; Foucart et al. 2016; Lehner et al. 2016a; Rezzolla & Takami 2016), confirming that the instability is triggered in all of them to some extent.

Since the power in the  $(2, 1)$ -mode reflects the asymmetry in the mass of the system, its power depends sensitively on the mass ratio, being almost a factor fifty smaller than the corresponding  $(2, 2)$ -mode in the case of equal-mass binaries (see left panel). It should be noted, however, that the power at the  $f_{m=1}$  frequency does not depend only on the strength of the  $m = 1$  deformation, and hence on the mass ratio, but also on the survival time of the remnant, which in turn depends on the spin of the binary. For example, in the case of the TNTYST binaries with the largest spin, i.e.,  $\chi_1 = 0.6$ , and which have a lifetime of at least 34.8 ms in all simulations, the strongest  $m = 1$  contribution is obtained for  $q = 0.8$  and not for  $q = 0.6$ . As expected, even in this specific high-spin case, the equal-mass binary has an  $f_{m=1}$  contribution that is smaller than that of the unequal-mass  $q = 0.8$  case, suggesting a non-monotonic response regarding the mass ratio. This behaviour seems to suggest that there exist an optimal mass ratio for the onset of the  $m = 1$  instability and that for very large mass asymmetries and stiff EOSs, the mass of the secondary is too small to produce significant  $m = 1$  deformations, thus leaving the  $m = 2$  bar-mode as the dominant deformation.

This conjecture is supported by the results obtained with the BHBA $\Phi$  binaries, even though the set of long-lived models available is more limited. Also in these binaries, in fact, and for the binaries with the largest primary spin  $\chi_1 = 0.6$ , the instability is triggered more strongly at  $q = 0.8$  compared to  $q = 0.6$ . This conclusion is more robust for binaries with a mass that is 2.5% above the irrotational threshold mass, and for which both models survive for at least 26.5 ms after merger. The same cannot be said for binaries with total masses at 5.0% above the threshold mass, where the  $q = 0.6$  binary unfortunately collapses already 8.4 ms after the merger.

We note that because the  $m = 1$  asymmetry introduced by the

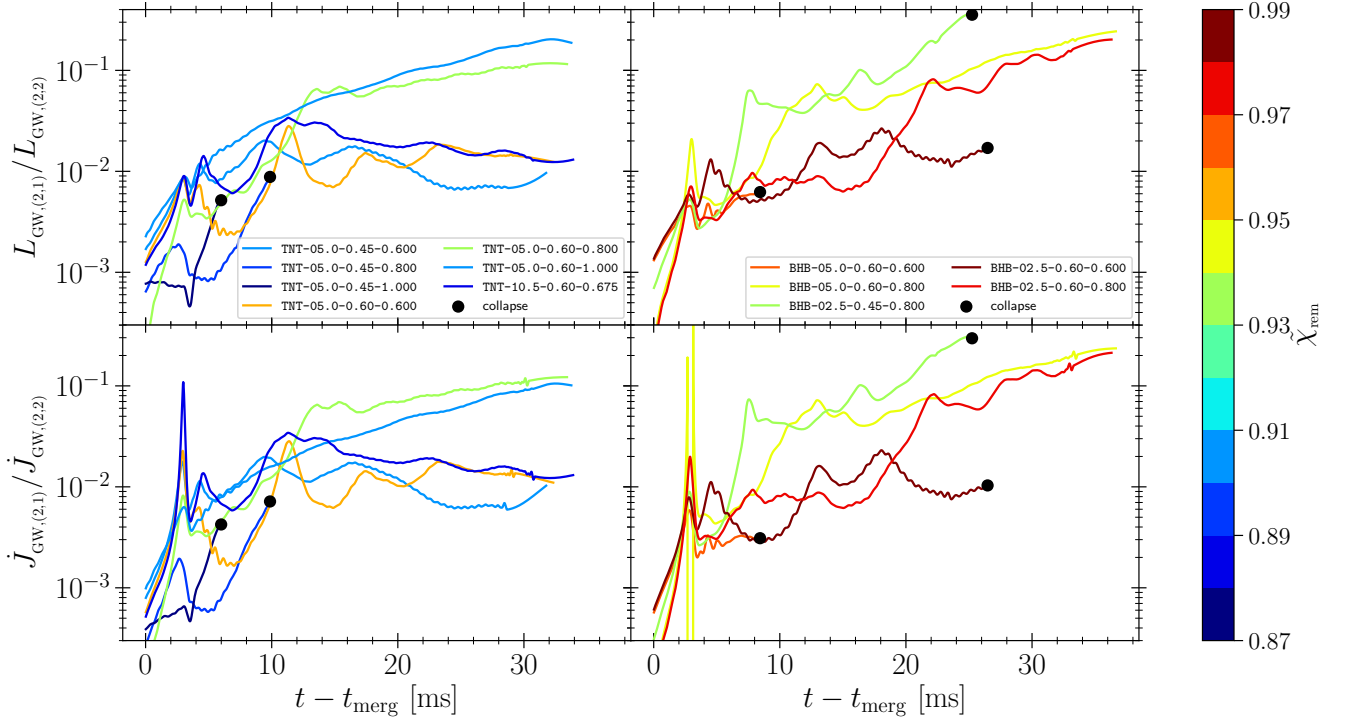


**Figure 4.** Left panel: Ratio of the evolution of the instantaneous GW luminosities in the two modes, i.e.,  $L_{\text{GW},(2,1)}/L_{\text{GW},(2,2)}$  (top parts) and the corresponding losses of angular momentum, i.e.,  $\dot{J}_{\text{GW},(2,1)}/\dot{J}_{\text{GW},(2,2)}$  (bottom parts), for the TNTYST EOS (left panel). Black circles mark the time of collapse of the remnant. Left panel: The same as in the left panel but for the BHBΛΦ EOS.

one-arm instability tends to be more long-lived than the  $m = 2$  bar-mode asymmetry triggered at merger by the large angular momentum of the remnant (Manca et al. 2007), the  $m = 1$  contribution grows for longer post-merger HMNS lifetimes, increasing its contribution to the GW emission. Over time, however, this growth levels off, so that the  $m = 1$  contribution remains at values that are of the order of  $\sim 1\%$  when compared to the  $m = 2$  emission over the timescales explored in our simulations. As an example, simulating the BHB-02.5-0.60-0.800 binary at a lower resolution of 295 m revealed that the remnant is potentially long-lived with a lifetime of at least 92 ms when neglecting any dissipative processes apart from GW radiation. In this case, the ratio of the GW strain amplitudes in the (2,1)- and (2,2)-mode varies with time reaching  $h_{21}/h_{22} \approx 5$  at the end of the simulation, thus indicating that the  $m = 1$  asymmetry is long-lived (Bernuzzi et al. 2014; Paschalidis et al. 2015; Radice et al. 2016a).

Figure 4 provides a synthetic overview of much of what just discussed. More specifically, it shows the ratio of the evolution of the instantaneous GW luminosities in the two modes, i.e.,  $L_{\text{GW},(2,1)}/L_{\text{GW},(2,2)}$  (top parts) and the corresponding losses of angular momentum, i.e.,  $\dot{J}_{\text{GW},(2,1)}/\dot{J}_{\text{GW},(2,2)}$  (bottom parts), for the TNTYST EOS (left panel) and for the BHBΛΦ EOS (right panel).

The actual values are computed from the Weyl scalar  $\Psi_4$  on a spherical surface at a distance of 735 km from the center of the system (see Eq. (117) and (119) in Bishop & Rezzolla 2016) and the evolution is deconvolved with a Savitzky-Golay filter (Savitzky & Golay 1964) to reduce the inevitable noise produced by the ratio of two rapidly varying quantities. Furthermore, black filled circles are used to mark the time of collapse of the remnant. Note that the ratio of the luminosities grows nonlinearly right after the merger and that, although the evolution of these GW quantities is not correlated

uniquely with the rescaled dimensionless spin,  $\chi_{\text{rem}}$ , the ratios reach values of  $\sim 0.01$  for binaries with small  $\chi_{\text{rem}}$ , and become  $\sim 0.1$  for binaries with large  $\chi_{\text{rem}}$ . Furthermore, in some cases, and just before collapse,  $L_{\text{GW},(2,1)}/L_{\text{GW},(2,2)}$  can be as large as 0.3. Given the length over which the simulations have been carried out, it remains unclear whether  $L_{\text{GW},(2,1)}/L_{\text{GW},(2,2)} \sim 1$  for those remnants with a lifetime spanning hundreds of milliseconds. Future, long-term simulations of these binaries will help settle this question.

To provide a more quantitative measure of the GW emissions for the different binaries, Tab. 3 reports the contributions of the dominant post-merger frequency  $f_2$  and the one-arm instability frequency  $f_{m=1}$  to the GW spectrum (see Fig. 3), collectively within an 5 ms time window after merger. In this way, it is possible to note that while the strain amplitude in the  $f_{m=1}$  may dominate over long timescales, the effective power poured into that mode at merger is nevertheless subdominant, being  $\leq 8\%$  for all the cases surviving long enough to be considered. The data in Tab. 3 also suggests that while the stiffness of the EOS plays a major role in the dynamics of the  $m = 1$  instability, it also shows that a highly spinning primary can change the response in the newly formed HMNS contrary to expectation from irrotational binary mergers. Especially the differences between  $\chi_1 = 0.45$  and  $\chi_1 = 0.6$  for TNTYST suggest the development of this instability depends sensitively on the combination of stiffness, spin and mass asymmetry. Moreover, the ratio between the two contributions,  $h_{\text{eff},f_{m=1}}/h_{\text{eff},f_2}$ , changes over time, as can be seen in Tab. 3, thus suggesting different damping timescales for the  $m = 2$  and the  $m = 1$  modes.

binary model	$h_{\text{eff},f_2}$	$h_{\text{eff},f_{m=1}}$	$\frac{h_{\text{eff},f_{m=1}}}{h_{\text{eff},f_2}}$	$\frac{h_{\text{eff},f_{m=1}}}{h_{\text{eff},f_2}} \Big _{5\text{ms}}$	$E_{\text{GW,tot}}$ [ $M_{\odot}$ ]	$J_{\text{GW,tot}}$ [ $M_{\odot}^2$ ]
TNT-10.5-0.60-0.675	0.500	0.032	0.064	0.173	0.05	0.97
TNT-10.5-0.60-0.838	0.764	0.028	0.036	0.037	0.07	1.31
TNT-05.0-0.45-0.600	0.414	0.032	0.078	0.131	0.03	0.60
TNT-05.0-0.45-0.800	0.682	0.023	0.034	0.030	0.08	1.54
TNT-05.0-0.45-1.000	1.000	0.019	0.019	0.021	0.07	1.35
TNT-05.0-0.60-0.600	0.428	0.028	0.065	0.104	0.03	0.67
TNT-05.0-0.60-0.800	0.594	0.033	0.056	0.341	0.05	1.09
TNT-05.0-0.60-1.000	0.895	0.031	0.035	0.019	0.06	1.33
BHB-05.0-0.60-0.600	0.333	0.019	0.057	0.042	0.02	0.52
BHB-05.0-0.60-0.800	0.371	0.029	0.079	0.295	0.03	0.84
BHB-02.5-0.45-0.800	0.404	0.030	0.075	0.267	0.03	0.76
BHB-02.5-0.60-0.600	0.377	0.021	0.056	0.108	0.03	0.66
BHB-02.5-0.60-0.800	0.428	0.027	0.063	0.169	0.04	0.96

**Table 3.** Contribution to the GW spectrum of the dominant post-merger frequency  $f_2$  (second column), of the one-arm instability frequency  $f_{m=1}$  (third column). Shown also are the ratio between these two quantities either over the whole lifetime (fourth column) or when integrated over a time window of 5 ms after merger (fifth column). Since all the binaries reported lead to remnants that are either medium- or long-lived, the window is chosen so as to cover all models equally. The values are normalized by the highest power in this summary, i.e., by the  $f_2$ -power of TNT-05.0-0.45-1.000. In addition the total post-merger radiated mass-energy  $E_{\text{GW,tot}}$  (sixth column) and angular momentum  $J_{\text{GW,tot}}$  (seventh column) are listed, measured up to collapse respectively the end of the simulation.

### 3.2 Asymmetry and lifetime of the remnant

In the following we will discuss the lifetime of the merger remnant before it collapses to a BH, distinguishing the results obtained for the TNTYST EOS from those of the BHB $\Lambda$  $\Phi$  results.

We start by recalling that the remnants of binary mergers with masses well above the maximum mass allowed by uniform rotation (Breu & Rezzolla 2016) are, with due exceptions, in a metastable equilibrium as they will eventually collapse to a system composed of a BH and an accreting torus (Baiotti & Rezzolla 2017). The lifetime of the remnant depends therefore on a number of properties of the binary, most notably, the total mass, the mass ratio, the spin of the constituents, and, of course, the EOS. The shortest lifetime is the one in which the collapse takes place within one free-fall timescale (Koeppel et al. 2019; Tootle et al. 2021) and can be estimated in a number of different ways (see also Agathos et al. 2020; Bauswein et al. 2020). We here follow the methodology first developed by Koeppel et al. (2019) and further refined to account for spin and unequal-mass systems by Tootle et al. (2021), in which the normalized minimum of the lapse  $\hat{\alpha}(t) = \alpha_{\text{min}}(t)/\max(\alpha_{\text{min}}(t))$  is used to compute the lifetime  $\tau_c$  and compares it to the freefall timescale. In this approach, the lifetime is then computed as the interval between the time of merger (defined as the one at which  $\hat{\alpha} = 0.9$ ) and the time of black-hole formation (defined as when  $\hat{\alpha} = 0.1$ ).

Once the timescale  $\tau_c$  is computed, we classify the post-merger lifetime in three main classes, with the understanding that this classification is in large part arbitrary and useful mostly to set some general qualitative behaviours. In particular, we consider the merger remnant to be: (i) *short-lived* if the remnant collapses over a timescale

$\tau_c \lesssim 5 \text{ ms}$ <sup>3</sup>. (ii) *medium-lived* if the remnant collapses over a timescale  $5 \lesssim \tau_c \lesssim 10 \text{ ms}$ . (iii) *long-lived* if the remnant collapses over a timescale  $\tau_c \gtrsim 10 \text{ ms}$ .

Concentrating on TNTYST configurations first, the long-lived remnants that have not collapsed by the end of the simulations, survive for at least 34.2 ms after merger. This applies to models TNT-10.5-0.60-0.675, TNT-05.0-0.45-0.600, TNT-05.0-0.60-0.600, TNT-05.0-0.60-0.800, and TNT-05.0-0.60-1.000, which, despite being 10.5% and 5.0% over  $M_{\text{th}}^{1,0}$ , do not show evidence of a collapse to a BH over these timescales. Additionally, the three models TNT-10.5-0.60-0.837, TNT-05.0-0.45-0.800 and TNT-05.0-0.45-1.000, lead to medium-lived remnants, undergoing a collapse after a timescale of  $\tau_c \simeq 5.7 \text{ ms}$ ,  $9.9 \text{ ms}$ , and  $6.0 \text{ ms}$  after merger, respectively. Finally, model TNT-10.5-0.45-0.675 results in a short-lived post-merger remnant ( $\tau_c \simeq 2.4 \text{ ms}$ ), indicating that this system is very close to a prompt collapse in terms of total mass.

To quantify the effect of the spin angular momentum of the primary on the lifetime of the remnant, we calculate the rescaled dimensionless angular momentum of the remnant at merger, which we define as

$$\tilde{\chi}_{\text{rem}} := \left( \frac{M_{\text{th}}^{1,0}}{M_{\infty}} \right) \frac{J_{\text{ADM}} - J_{\text{GW}}}{(M_{\text{ADM}} - M_{\text{GW}})^2}, \quad (1)$$

where  $J_{\text{ADM}}$  is the total ADM angular momentum and  $M_{\text{ADM}}$  the total ADM mass of the initial data. Furthermore, since the system is losing both angular momentum,  $J_{\text{GW}}$ , and (gravitational) mass,  $M_{\text{GW}}$ , via the emission of GWs, these need to be removed from the estimate of  $\tilde{\chi}_{\text{rem}}$ . Both  $J_{\text{GW}}$  and  $M_{\text{GW}}$  are computed from the Weyl scalar  $\Psi_4$  on a spherical surface at a distance of 735 km from the center of the system (see e.g., Bishop & Rezzolla 2016) and are integrated in time from the start of the simulations and up to the merger. Because of this,  $J_{\text{GW}}$  and  $M_{\text{GW}}$  do not contain the contributions radiated before the start of the simulation, instead these are already correctly incorporated within  $J_{\text{ADM}}$  and  $M_{\text{ADM}}$  by the underlying assumption of quasi-circularity of the initial data. In addition, we employed a rescaling by the mass criticality  $M_{\text{th}}^{1,0}/M_{\infty}$  to introduce a dependency of super-criticality in the mass of the binary. While this choice is arguably arbitrary, it has been introduced to reflect the fact that the various models considered are above the irrotational threshold mass at different degree, and this has an impact on the survival time of the merger remnant quite independently of the magnitude of the angular momentum at merger alone. Without this correction, it would be difficult to distinguish the contribution to the remnant lifetime that is introduced by the large spin of the system and by a comparatively small mass; indeed, without this correction, Fig. 5 would not show a distinct systematic behaviour it shows now (see below for a detailed discussion).

All in all, the total dimensionless angular momentum of the remnant given by expression (1) provides an estimate of how much angular momentum is in the remnant object at the time of the merger. Since  $J_{\text{GW}}$  and  $M_{\text{GW}}$  can be estimated reasonably well with post-Newtonian expressions,  $\tilde{\chi}_{\text{rem}}$  is in principle a quantity that can be estimated directly from the observations.

As already noted in Sec. 3.1, the systems experience longer inspirals with increasing spin of the primary due to the spin-orbit coupling and the net increased angular momentum. This not only leads to differing merger times for the same total mass  $M_{\infty}$ , but also to different

<sup>3</sup> Given that the free-fall timescale is below one millisecond for standard values of neutron-star compactness, short-lived remnants include also those undergoing prompt collapse.

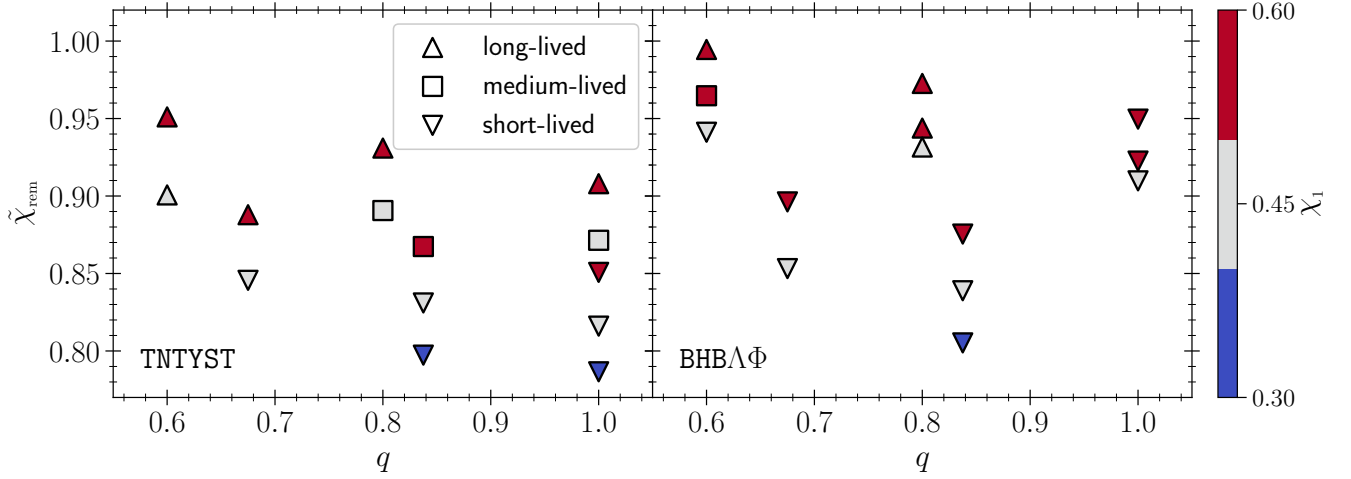


**Figure 5.** *Left panel:* Rescaled dimensionless spin angular momentum of the remnant at merger [Eq. (1)] shown as a function of the mass ratio for the TNTYST binaries. Upward-pointing triangles refer to the long-lived remnants, squares to the medium-lived ones, while short-lived remnants are indicated with downward-pointing triangles (see Sec. 3.2 for a definition). Also indicated with a colourcode is the spin of the primary (see also Tab. 1). *Left panel:* The same as in the left panel but for the BHB $\Lambda\Phi$  EOS.

$\chi_{\text{rem}}$  at merger (see also Dietrich et al. 2015, 2017b). A synthetic view of the total dimensionless angular momentum at merger is presented for both EOSs and as a function of the mass ratio in Fig. 5, where the upward-pointing triangles refer to the long-lived remnants, the squares to the medium-lived ones, while short-lived remnants are indicated with downward-pointing triangles. Also indicated with a colourcode is the spin of the primary. As expected, the systems with primary stars having larger  $\chi_1$  show an increased  $\chi_{\text{rem}}$  at merger.

In the case of the softer TNTYST EOS, the left panel of Fig. 5 illustrates rather clearly that the spin in the primary has the net effect of increasing the lifetime of the remnant, so that all long-lived remnants are those having large values of  $\chi_1$ . Interestingly, the spin of the remnant as defined by Eq. (1) seems to cluster approximately into three different regions:  $\bar{\chi}_{\text{rem}} \gtrsim 0.90$  for long-lived remnants,  $0.86 \lesssim \bar{\chi}_{\text{rem}} \lesssim 0.90$  for remnants that can be either long- or medium-lived, and  $\bar{\chi}_{\text{rem}} \lesssim 0.86$  for remnants that are short-lived. We also note that, in contrast to what has been found by concentrating on the threshold mass of irrotational binaries with significant mass ratio (Bauswein et al. 2017, 2020, 2021; Bernuzzi et al. 2020) and in line with the findings in Tootle et al. (2021) for  $|\chi_1| \leq 0.3$ , we find that with a significantly spinning primary, the effective threshold mass grows with increasing mass asymmetry for TNTYST (see the survival times in Tab. 1).

What discussed so far continues to hold also for the stiffer BHB $\Lambda\Phi$  EOS, although not without some important differences. Also in this case, in fact, all long-lived remnants follow from binaries having a rapidly spinning primary. Furthermore, the spin of the remnant at merger is again larger in the presence of large mass asymmetries. However, there are notable differences comparing the right to the left panel of Fig. 5. First,  $\bar{\chi}_{\text{rem}}$  exhibits overall a larger spread, second, there is a clear exception from the trend identified above with the TNTYST EOS, namely, that for equal-mass binaries a very rapidly spinning primary does not prevent the merger remnant to be short-lived. The fact that this behaviour is found for the BHB $\Lambda\Phi$  EOS only indicates that the impact of the spin is less important in equal-mass mergers with stiff EOSs. On the other hand, what is even more relevant for this EOS is that it is much harder to find binaries with medium-lived remnants. Indeed, the simulated systems exhibit mostly remnants that are either short-lived (nine out of 14 bina-

ries) or long-lived (four out of 14 binaries). Only in one instance, i.e., BHB-05.0-0.60-0.600, does the remnant survive for 8.4 ms before collapsing. Not surprisingly, the few long-lived remnants, i.e., the models BHB.050.0.60-0.800, BHB.025.0.45-0.800, BHB.025.0.60-0.600 and BHB.025.0.60-0.800 (the corresponding HMNSs survive at least for 25.2 ms for these models), also correspond to those binaries that have masses only up to 5% above the threshold mass for irrotational binaries. This result underlines how the lifetime of the remnant can be increased if the system has large mass asymmetries, a primary with a large spin, and is not excessively massive. Indeed, for the binary BHB.025.0.60-0.800, the remnant shows long-term lifetime of at least 92.0 ms in the lower-resolution simulation (see discussion in Sec. 3.1).

As anticipated in Sec. 3.1, the lifetime of the merger remnant has an impact on the GW spectrum and on the relative importance of the  $m = 1$  and  $m = 2$  deformations. At the same time, reading off such importance from the amplitude of the  $f_{m=1}$  and  $f_2$  peaks in Fig. 3 can be misleading, because they reflect different lifetimes of the merger remnant. This can be accommodated by considering the emitted power within a precise window in time, e.g., 5 ms as reported in Tab. 3, as in this case all models are evaluated equally. Doing so highlights that for the TNTYST EOS models, a smaller mass ratio (and therefore a larger mass asymmetry) leads to a comparatively larger  $m = 1$  emission and to longer lifetimes<sup>4</sup>. This indicates that – for a given mass and spin – a small mass ratio leads to a weakening of the  $m = 2$  deformation, which, in turn, produces a reduced loss of GWs and angular momentum, and thus a longer lifetime. At the same time – for a given mass and mass ratio – a larger spin unambiguously increases the remnant lifetime (see the values of  $\tau_c$  in Tab. 1).

The role played by the mass asymmetry in the merger remnant and the impact it has on its lifetime can be appreciated from Fig. 2, when comparing the rest-mass density of the binaries

<sup>4</sup> We note that, strictly speaking, the equal-mass binaries with the TNTYST EOS are also those that lead to the largest amounts of radiated GW energy (see Tab. 3). These binaries, however, are short lived and the  $m = 1$  does not have sufficient time to provide a large contribution as it is the case for binaries with larger mass asymmetry.

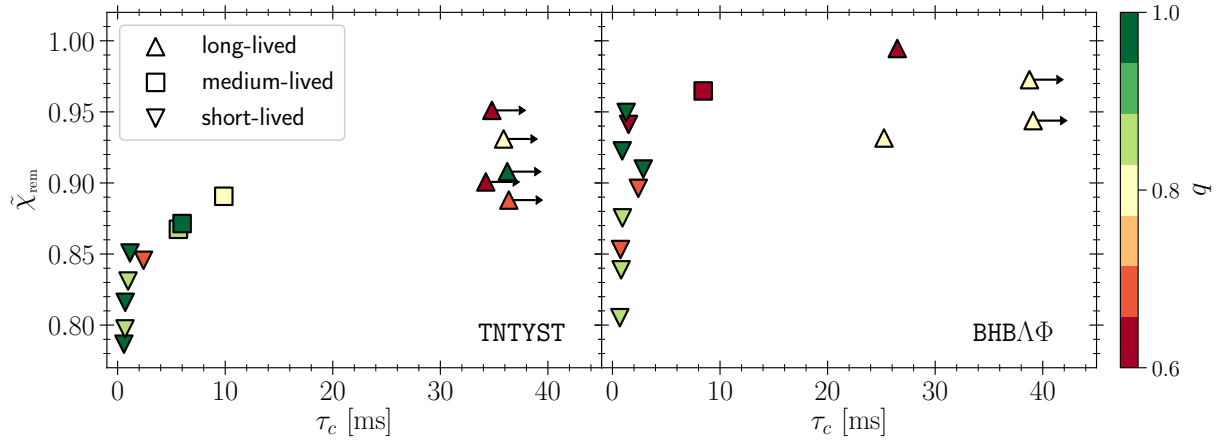


**Figure 6.** *Left panel:* Rescaled dimensionless spin angular momentum of the remnant at merger [Eq. (1)] shown as a function of the remnant lifetime  $\tau_c$  for the TNTYST binaries. Upward-pointing triangles refer to the long-lived remnants, squares to the medium-lived ones, while short-lived remnants are indicated with downward-pointing triangles (see Sec. 3.2 for a definition). Also indicated with a colourcode is the mass ratio  $q$  of the binary. *Left panel:* The same as in the left panel but for the BHB $\Lambda\Phi$  EOS.

TNT-05.0-0.45-0.800 (top panels) and TNT-05.0-0.60-0.800 (bottom panels), which differ only in the spin of the primary. These two binaries show a large difference in both the HMNS lifetime (which is at four times larger for  $\chi_1 = 0.45$  than for  $\chi_1 = 0.6$ , with the former not collapsing until the end of the simulation) and the ratio of the  $m = 1$  and  $m = 2$  GW emissions (which is of factor 10 within the first 5 ms, that is, almost twice as large for  $\chi_1 = 0.6$  than for  $\chi_1 = 0.45$ ). In both cases, the remnant exhibits an asymmetry in the density distribution, which however are dissipated more rapidly in the less-spinning binary  $\chi_1 = 0.45$ , whose core assumes an almost axisymmetric distribution after about 9 ms. On the other hand, the mass asymmetry is more long-lived for the highly spinning binary with  $\chi_1 = 0.6$  and is indeed present until the end of the simulation at  $t - t_{\text{mer}} = 35.9$  ms. Clearly, the asymmetry in this case will lead to a persistent GW emission in the  $m = 1$  mode.

A similar behaviour is exhibited also by the binaries of the BHB $\Lambda\Phi$  EOS, with the most relevant difference being that the lifetime of the remnant in this case is maximised not for the binaries with the smallest mass ratio, but rather with an intermediate one. Once again, this is related to the ability of triggering a long-lasting asymmetry in the remnant, able to produce GW at a reduced rate and thus, in conjunction with larger  $\chi_{\text{rem}}$ , increase its lifetime.

In summary, the results presented in this section suggest that the properties of the merger remnant, most notably its degree of asymmetry in the rest-mass distribution and its lifetime, depend on a subtle balance between the mass of the binary, the mass ratio, and the spin of the primary. In this complex combination, long-lived remnants tend to be systematically associated to large dimensionless spins at merger. However, while for binaries with softer EOSs this happens at the smallest mass ratios, namely, at  $q = 0.6$  for the TNT EOS, for binaries with stiffer EOSs this happens at an intermediate mass ratio, namely, at  $q = 0.8$  for the BHB $\Lambda\Phi$  EOS.

All of this is nicely summarised in Fig. 6, which reports the rescaled dimensionless spin angular momentum at merger  $\chi_{\text{rem}}$  for the TNTYST (*left*) and the BHB $\Lambda\Phi$  (*right*) binaries shown as a function of the remnant lifetime  $\tau_c$ . The symbol notation is the same as in previous figures (see Table 1) and distinguishes between long-, medium- and short-lived remnants; also indicated with a colourcode is the mass ratio  $q$  of the binary. Note how both panels indicate that the lifetime increases with the dimensionless spin and that this

dependence can be considerably nonlinear especially for remnants that are short- or medium-lived. Furthermore the long-lived remnants are also those with the largest dimensionless spin at merger, thus pointing out that the ability of storing angular momentum in the remnant represents the most efficient way to extend the lifetime of the merger product. Finally, note that the longest lived remnants are normally those with the smallest mass ratio in the case of the soft EOS TNTYST, i.e.,  $q = 0.6$ . However, this is not the case for the stiffer BHB $\Lambda\Phi$  EOS, where the longest-lived remnants are actually those with intermediate mass ratio, i.e.,  $q = 0.8$ . This is an interesting demonstration that, as mentioned above, the lifetime of the merger remnant is a complex balance between mass, mass ratio, spin, and EOS properties. While this is true also for the threshold mass to prompt collapse  $M_{\text{th}}$ , where the work of Tootle et al. (2021) has shown that it is even possible to describe a quasi-universal behaviour of  $M_{\text{th}}$  as a function of  $q$  and  $\chi_1$ , the properties of the remnant lifetime appear more complex and hence more difficult to describe in terms of a simple quasi-universal behaviour. This is not particularly surprising given the complex nonlinear dynamics that follows the merger and the development of instabilities of various type, some of which, (e.g., those associated with the presence of strong magnetic fields) are ignored here.

### 3.3 Dynamical ejecta and remnant disc mass

We next discuss how to use the simulations to estimate the remnant disc – both when the merger product collapses to a BH and when it is long-lived – and the dynamically ejected mass for of all binaries considered. Both of these quantities are essentials to put constraints on the observable characteristics of these systems and hence on their multi-messenger appearance. Numerical values for the disc masses can be found in Tab. 1, while the dynamical ejecta together with their average properties are collected in Tab. 4.

We have estimated the disc masses via two different methods, depending on whether the remnant undergoes a collapse to a BH or stays metastable within the given simulation times. In the former case, the disc mass is calculated by integrating over the conserved rest-mass density except for the volume within the apparent horizon; in the latter case, instead we select a cut-off rest-mass density of  $10^{13}$  g/cm<sup>3</sup> and thus exclude from the integral the matter contribution within the

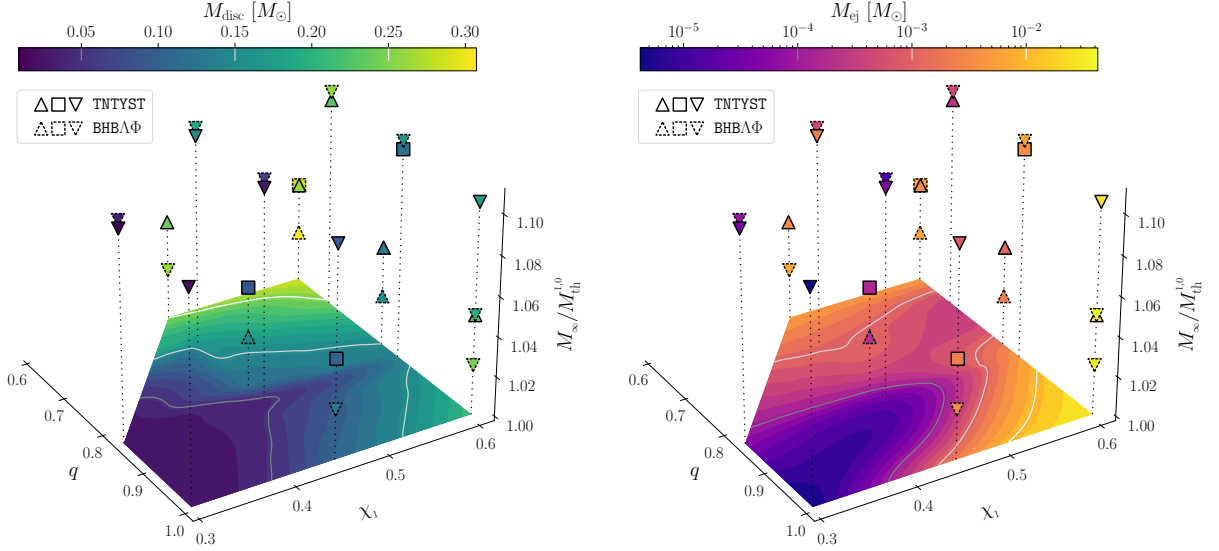


**Figure 7.** *Left panel:* Remnant disc masses,  $M_{\text{disc}}$ , for both EOSs shown with a colourcode as function of the dimensionless spin of the primary  $\chi_1$ , of the mass ratio  $q$ , and of the the mass criticality  $M_{\infty}/M_{\text{th}}^{1.0}$  (the latter represents the vertical axis). The different symbols follow the convention presented in Tab. 1 and refer to the different lifetime of the remnants. Shown on the horizontal plane is a cubic spline interpolation of the data, where an average is performed for all models at fixed mass ratio and primary spin. The projection also reports isocontours of  $M_{\text{disc}}$  at  $0.05, 0.15, 0.25 M_{\odot}$ . *Right panel:* The same as the left but reporting the dynamically ejected mass  $M_{\text{ej}}$ . The projection on the horizontal plane reports isocontours of  $M_{\text{ej}}$  at  $10^{-4}, 10^{-3}, 10^{-2} M_{\odot}$ .

HMNS (see e.g., Hanauske et al. 2017; Radice et al. 2018b). We note that because matter is still undergoing accretion onto the BH or is settling into a quasi-steady state around the HMNS after the merger, we compute the disc masses either 5 ms after collapse in the first scenario, or 15 ms after merger in the second one. Of course this choice is somewhat arbitrary and brings in a certain error, as the disc mass estimates reach a genuine stationary value only on much longer time-scales, where disc-ejection mechanisms will start to dominate (see Metzger 2017; Gill et al. 2019, for a review). We estimate this error in the disc mass related to this choice to be  $\approx 10 - 20\%$ .

The left panel of Fig. 7 shows with a colourcode the disc masses  $M_{\text{disc}}$  as a function of the primary spin  $\chi_1$ , of the mass ratio  $q$ , and of the mass criticality  $M_{\infty}/M_{\text{th}}^{1.0}$ , shown as the vertical axis. The symbol notation is the same as in Tab. 1 and is used to distinguish short-, medium- and long-lived remnants, with solid symbols referring to the TNTYST EOS, while dashed ones are used for the BHBA $\Phi$  EOS.

A number of interesting behaviours appear quite clearly from the left panel of Fig. 7 and apply equally to the TNTYST and BHBA $\Phi$  EOSs. First, the smallest disc masses are attained for binaries having low spin in the primary; clearly, even smaller disc masses would be expected for binaries with  $\chi_1 = 0.0$  (not shown in Fig. 7). Second, and by contrast, the largest disc masses are reached for binaries having small mass ratios and high spin in the primary; under these conditions, discs with masses well above  $0.1 M_{\odot}$  are possible for both EOSs and would lead to a significant contribution to the matter ejected secularly since some of these models lead to a long-lived remnant (see discussion in sec. 3.4). Third, the disc masses can be considerably different between the high- and low-spin systems, varying by almost three orders of magnitude for the TNTYST EOS and the binary with mass criticality  $M_{\infty}/M_{\text{th}}^{1.0} = 1.105$ . Fourth, for low-spin binaries, i.e.,  $\chi_1 = 0.3$ , the variation in disc mass with mass ratio is very mild and  $\lesssim 30\%$ ; this is not the case for rapidly spinning primaries, i.e.,  $\chi_1 = 0.45$ , where the variation in disc mass with  $q$  can be  $\gtrsim 50\%$ . Finally, and interestingly, a local minimum appears

for  $q = 0.8$  and highly spinning binaries, i.e.,  $\chi_1 = 0.6$ , once again pointing out that the combined impact of mass ratio and spin is not trivial and can lead to non-monotonic behaviours of the disc mass in highly spinning binaries. An analytic modelling of the disc masses as a function of the mass ratios and spins of the binaries will be discussed in a forthcoming work.

Following in a similar fashion, the right panel of Fig. 7 provides a synthetic summary of the mass that is ejected dynamically using the same convention employed in Fig. 7; more precise numerical values of the ejected mass can also be found in Tab. 4 alongside with the average electron fraction  $\langle Y_e \rangle$ , velocity at infinity  $\langle v \rangle_{\text{ej}}$ , and entropy per baryon  $\langle s \rangle$ . The table also reports the total ejected mass  $M_{\text{tot}}$ , which we define as the sum of the dynamically ejected mass and of a fraction of the rest-mass of the remnant disc, i.e.,

$$M_{\text{tot}} := M_{\text{ej}} + \frac{1}{2} M_{\text{disc}}, \quad (2)$$

where the disc mass is expected to be ejected secularly via a number of physical processes such as neutrino or magnetically driven winds (see Gill et al. 2019, for a summary of these secular winds).

Also in the case of the dynamically ejected matter, a number of interesting behaviours can be deduced from the right panel of Fig. 7 and apply to both EOSs. First, the smallest values of the ejecta are attained for binaries having equal masses and low spin in the primary; clearly, even smaller ejected masses would be expected for binaries with  $q = 1, \chi_1 = 0.0$  (not shown in Fig. 7). Second, considerably larger ejecta are reached for binaries having small mass ratios and high spin in the primary; under these conditions, the ejected mass can be of the order of  $10^{-3} M_{\odot}$  for both EOSs (see Tab. 4). Third, and differing from what seen for the disc mass, the largest amounts of ejected matter are attained for equal-mass, rapidly spinning binaries; more specifically for  $q = 1$  and  $\chi_1 = 0.6$ , the dynamically ejected mass can be of the order of  $10^{-2} M_{\odot}$  for both EOSs, yielding a total ejected mass in excess of  $0.1 M_{\odot}$  (see Tab. 4). Finally, we report again evidence for a non-monotonic behaviour of the ejected mass

when moving across different mass ratios and for binaries with fixed spin.

When examining the additional average properties of the ejecta presented in Tab. 4, e.g., the average electron fraction  $\langle Y_e \rangle$ , the average velocity at infinity  $\langle v \rangle_{\text{ej}}$ , the average entropy  $\langle s \rangle$  together with the derived quantities, it is possible to appreciate that they lie within the typical range for rather cold, very neutron-rich and fast ejecta, typically found in quasi-circular BNS mergers (see e.g., Radice et al. 2016b; Bovard et al. 2017). The most relevant difference can be found in those configurations showing a comparatively larger entropy, velocity or composition. In these cases, the tidal tails and remnant matter from the tidal disruption, undergo a multitude of interactions. Most notably, the matter ejected from the spinning primary expands faster thanks to the inherent large angular momentum; in turn, this implies that in some cases the expanded matter shocks with the elongated matter tails produced by the tidal disruption, thus leaving potential imprints on the properties of the ejecta.

### 3.4 Implications on the kilonova emission

The results discussed in the previous section on the disc mass and ejected matter have a direct impact on the electromagnetic counterpart to the BNS merger and, in particular, on the kilonova emission. To discuss such implications, it is useful to distinguish the case of short-lived remnants from that of the long-lived ones.

In the first case, namely, for binaries leading to a short-lived remnant but retaining a large amount of dynamical ejecta and a massive remnant disc, the kilonova emission is expected to contain merely a red component. Simulations concentrating on matter ejection from the disc around a remnant BH have shown that up to 40% of the disc mass can be ejected at average velocities of  $\langle v \rangle \approx 0.1c$  and electron fraction of  $\langle Y_e \rangle \approx 0.2$  (Siegel & Metzger 2017, 2018; Fernández et al. 2019; Christie et al. 2019). However, it is not clear yet if these results with initial disc masses of  $\approx 0.03 M_\odot$  can be scaled to massive discs as those obtained in many of our configurations. The low electron fraction and moderate velocities of the dynamical ejecta found in our simulations for these configurations argue for a pure red kilonova. Indeed, we find that the dynamically ejected part of the outflow averages around  $\langle v \rangle \approx 0.14$  and  $\langle Y_e \rangle \approx 0.06$ , so that we assume here that both components evolve as a single red component. Furthermore, an electron fraction  $Y_e \approx 0.2$  from the secular disc ejecta is small enough to enable a robust r-process and thus lanthanide-rich ejecta (see e.g., Tanaka et al. 2018).

On the other hand, in the second case, namely, for binaries leading to a long-lived remnant, we expect that our results could have an impact especially in those cases where a large disc mass is produced and has sufficient time to lose a considerable part of in terms of ejected matter (these binaries, we recall, are those with small mass ratio and rapidly spinning primary). Under these conditions, the continuous neutrino irradiation, the asymmetries in the disc, as well as further outflows from the HMNS itself could influence the bulk properties of the kilonova emission. To capture these processes correctly, expensive high-resolution long-term simulations of the post-merger HMNS and disc are necessary (Metzger & Fernández 2014; Perego et al. 2014; Fujibayashi et al. 2017; Fujibayashi et al. 2018). Carrying out such simulations for the configurations considered here would yield very similar electromagnetic emissions with a blue component as for systems at lower masses (Wollaeger et al. 2018; Kawaguchi et al. 2018; Even et al. 2020; Korobkin et al. 2021; Wollaeger et al. 2021), but in combination with a potentially unexpectedly high chirp mass, hinting either to a highly spinning companion, an extreme mass asymmetry or both.

As a way to estimate the most salient characteristics of a single-component kilonova signal, a number of semi-analytical models have been developed by Grossman et al. (2014) and Wollaeger et al. (2018) to estimate the time of peak emission  $t_p$ , the corresponding peak bolometric luminosity  $L_p$ , and its effective temperature  $T_p$ . We here assume a grey opacity of  $10 \text{ cm}^2/\text{g}$ , which leads to a good agreement of the peak characteristics for ejecta undergoing a thorough r-process computed with more sophisticated modelling (Wollaeger et al. 2018). Furthermore, lacking a robust and universal estimate, we consider as a reference value that 50% of the disc rest-mass is ejected and at an average velocity of  $\langle v \rangle_{\text{disc}} = 0.1$ . We recall that the total ejected mass  $M_{\text{tot}}$  is the sum of the dynamical and disc ejecta [cf., Eq. (2)] and we use these two distinct masses obtain mass-weighted average velocity

$$\langle v \rangle := \frac{\langle v \rangle_{\text{ej}} M_{\text{ej}} + \frac{1}{2} \langle v \rangle_{\text{disc}} M_{\text{disc}}}{M_{\text{tot}}}, \quad (3)$$

The resulting characteristics of the kilonova emission are listed in Tab. 4, which includes long-lived remnants (indicated between round brackets) and for which the unknown lifetime of the remnant can potentially have large impact on the composition of the secular ejecta leading to more intricate emission features (Wollaeger et al. 2018; Even et al. 2020; Korobkin et al. 2021). At the same time, Fig. 8 reports, as a function of the total dimensionless spin of the merger remnant, the time of the peak (top part) and the luminosity at peak emission (lower part) for binaries modeled either with the TNTYST EOS (left panel) or with the BHBAΦ EOSs (right panel). Different symbols follow the remnant lifetime convention presented in Tab. 1 and the corresponding mass ratio in the binary is shown with a colourcode.

Notwithstanding the inherent scattering of the data, Fig. 8 clearly shows that there is a nonlinear correlation between the peak properties of the kilonova emission and the dimensionless spin of the remnant at merger. More specifically, large spins will systematically lead to peak times  $t_p$  taking place up to one day later and to luminosities  $L_p$  that are up to a factor five larger. Not surprisingly, these later peaks and larger luminosities correspond to models that are long-lived and could survive also beyond the timescale of our simulations. Hence, these values are to be interpreted only as lower limits both for  $t_p$  and  $L_p$ . Interestingly, because small mass ratios, i.e.,  $q = 0.6$ , are in general needed to produce long-lived remnants, it is such configurations that lead to the largest peak times and luminosities. Finally, for the BHBAΦ EOS, the intermediate mass ratios, i.e.,  $q \approx 0.84$ , yield the smallest values of  $t_p$  and  $L_p$ ; such a clear behaviour is not found in the TNTYST EOS, for which also equal mass binaries,  $q = 1$ , can be similarly less luminous and peak early.

Overall, and at least for this simplified modelling, the main source of variation in determining the characteristics properties of the kilonova emission is represented by the total ejected mass. Further differences could emerge from long-lived remnants, though the lifetime of the surviving merger remnants is unknown and hence no definitive conclusions can be found for these systems. Whereas these simple estimates show that there is an appreciable variation in the kilonova emission as a result of extreme spins and mass ratios, the maximum relative difference for binaries with the same total mass is well within the uncertainties of kilonova modelling, e.g., concerning opacities and especially morphology of the ejecta (Wollaeger et al. 2018; Even et al. 2020; Korobkin et al. 2021). This clearly calls for improved modelling of the actual kilonova emission.

binary model	$M_{\text{ej}}$ [ $10^{-2} M_{\odot}$ ]	$\langle Y_e \rangle$	$\langle v \rangle_{\text{ej}}$ [c]	$\langle s \rangle$ [ $k_{\text{B}}$ /baryon]	$M_{\text{tot}}$ [ $10^{-1} M_{\odot}$ ]	$\langle v \rangle$ [c]	$t_p$ [d]	$L_p$ [ $10^{40}$ erg/s]	$T_p$ [K]
TNT-10.5-0.30-0.837	0.0031	0.14	0.20	18.9	0.047	0.101	0.78	2.03	3880
TNT-10.5-0.30-1.000	0.0004	0.10	0.11	43.1	0.097	0.100	0.99	2.77	3725
TNT-10.5-0.45-0.675	0.2131	0.08	0.21	8.1	0.783	0.103	1.89	6.89	3323
TNT-10.5-0.45-0.837	0.0051	0.13	0.19	25.3	0.149	0.100	1.13	3.33	3639
TNT-10.5-0.45-1.000	0.0843	0.04	0.13	5.8	0.469	0.101	1.63	5.43	3417
TNT-10.5-0.60-0.675	0.0233	0.06	0.11	13.6	(1.142)	(0.100)	(2.17)	(7.90)	(3254)
TNT-10.5-0.60-0.837	0.3597	0.04	0.14	4.9	0.627	0.102	1.77	6.23	3363
TNT-10.5-0.60-1.000	2.6884	0.04	0.17	1.5	1.153	0.116	2.00	8.87	3257
TNT-05.0-0.45-0.600	0.3517	0.05	0.14	5.1	(1.239)	(0.101)	(2.21)	(8.25)	(3239)
TNT-05.0-0.45-0.800	0.0156	0.13	0.16	21.2	0.444	0.100	1.60	5.29	3427
TNT-05.0-0.45-1.000	0.2335	0.07	0.16	7.5	0.525	0.103	1.67	5.80	3397
TNT-05.0-0.60-0.600	0.3365	0.05	0.14	5.1	(1.347)	(0.101)	(2.27)	(8.54)	(3225)
TNT-05.0-0.60-0.800	0.1234	0.04	0.12	6.0	(0.701)	(0.100)	(1.85)	(6.44)	(3342)
TNT-05.0-0.60-1.000	2.8262	0.04	0.16	1.6	(1.438)	(0.112)	(2.18)	(9.53)	(3217)
BHB-10.9-0.30-0.837	0.0079	0.12	0.20	14.6	0.174	0.100	1.19	3.55	3609
BHB-10.9-0.45-0.675	0.0448	0.04	0.11	6.3	0.942	0.100	2.04	7.28	3288
BHB-10.9-0.45-0.837	0.0013	0.10	0.12	34.5	0.327	0.100	1.46	4.64	3485
BHB-10.9-0.60-0.675	0.0430	0.05	0.12	9.4	1.300	0.100	2.26	8.35	3231
BHB-10.9-0.60-0.837	0.5922	0.03	0.14	2.4	0.870	0.102	1.96	7.17	3304
BHB-05.0-0.60-0.600	0.6126	0.04	0.12	3.4	1.509	0.101	2.36	8.96	3204
BHB-05.0-0.60-0.800	0.1959	0.03	0.12	3.9	(0.812)	(0.100)	(1.94)	(6.85)	(3315)
BHB-05.0-0.60-1.000	4.2371	0.05	0.17	0.9	1.381	0.120	2.06	9.89	3226
BHB-02.5-0.45-0.600	0.7048	0.04	0.11	2.6	1.382	0.101	2.30	8.61	3220
BHB-02.5-0.45-0.800	0.0189	0.14	0.13	24.0	0.732	0.100	1.88	6.54	3334
BHB-02.5-0.45-1.000	0.3071	0.04	0.13	3.6	0.674	0.101	1.82	6.37	3350
BHB-02.5-0.60-0.600	0.6491	0.04	0.12	3.2	1.601	0.101	2.40	9.19	3194
BHB-02.5-0.60-0.800	0.2362	0.03	0.12	3.7	(0.792)	(0.101)	(1.92)	(6.79)	(3320)
BHB-02.5-0.60-1.000	3.0570	0.04	0.17	1.0	1.537	0.113	2.22	9.86	3205

**Table 4.** Average properties of the dynamical ejecta and of the kilonova-emission characteristics for all of the binaries evolved. Listed are the total dynamically ejected mass  $M_{\text{ej}}$ , the average electron fraction  $\langle Y_e \rangle$ , the average velocity at infinity  $\langle v \rangle_{\text{ej}}$ , the average entropy  $\langle s \rangle$ , the total ejecta  $M_{\text{tot}}$ , the mass-weighted ejecta velocity  $\langle v \rangle$ , the peak epoch of the kilonova emission  $t_p$ , the peak bolometric luminosity  $L_p$ , and the effective temperature at the peak  $T_p$ . The results for the long-lived remnants are given between round brackets due to the unknown remnant lifetimes.

## 4 DISCUSSION

We have investigated the effect of a highly spinning primary companion on the merger dynamics of high-mass BNS, being the physically more relevant scenario involving high spin states, where the primary NS was spun-up throughout the preceding binary evolution by accretion processes. For these we concentrated on configurations with total masses of up to  $\approx 11\%$  above their irrotational threshold mass for two fully temperature-dependent nuclear equations of state, i.e., TNTYST and BHB $\Lambda\Phi$ , being in the range of radii and maximum masses compatible with GW170817 (Most et al. 2018; Nathanael et al. 2021). In this way, we were able to cover for the first time both the space of parameters ranging from equal-mass to highly asymmetric binaries with mass ratio  $q = 0.6$ , and the space of parameters of rapidly spinning binaries with spin aligned with the orbital angular momentum, and where the primary has dimensionless spin ranging from  $\chi_1 = 0.3$  to  $\chi_1 = 0.6$ .

By performing fully general-relativistic hydrodynamic simulations of the inspiral, merger and post-merger of these systems, we were able to highlight a number of interesting aspects of the dynamics of these binaries. In particular, attention has been paid to the development of asymmetries in the mass distribution of the merger remnant. Besides the standard (2,2) bar-mode deformation, many remnants have exhibited also an (2,1) asymmetry, which is an effective indicator of the development of an  $m = 1$  instability. In particular,

such an instability has been found to provide sizeable contributions to the GW spectrum for all of the unequal-mass binaries, although these contributions remain subdominant (by one or more orders of magnitude) with respect to the (2,2) bar-mode deformation. Furthermore, depending on the EOS, the largest (2,1) asymmetry can be reached for the smallest mass ratio ( $q = 0.6$ ) in the case of the softer TNTYST EOS, or for an intermediate one ( $q = 0.8$ ) for the BHB $\Lambda\Phi$  EOS. Notwithstanding its smaller contribution on the timescales over which the simulations have been carried out, the (2,1) deformation appears to be less affected by dissipation, so that the corresponding emission from the  $m = 1$  GW emission could provide sizeable, if not comparable contributions for those binaries with large mass asymmetry and whose remnants can be long-lived.

Our simulations have also revealed a number of interesting aspects of the properties of the merger remnant, of its lifetime, of the mass in its disc, and of the ejected mass. All of these aspects can be briefly summarised as follows.

- The spin the primary can have a significant effect on the lifetime of the remnant even in the case of binaries with masses that significantly supercritical, i.e., with  $M_{\infty} \approx 1.1 M_{\text{th}}^{1.0}$ . In particular, a sufficiently large dimensionless angular momentum at merger is able to systematically yield remnants that are long-lived.
- Binaries with significant mass asymmetry with  $q \approx 0.6 - 0.8$ , tend to systematically yield remnants that are longer-lived than those

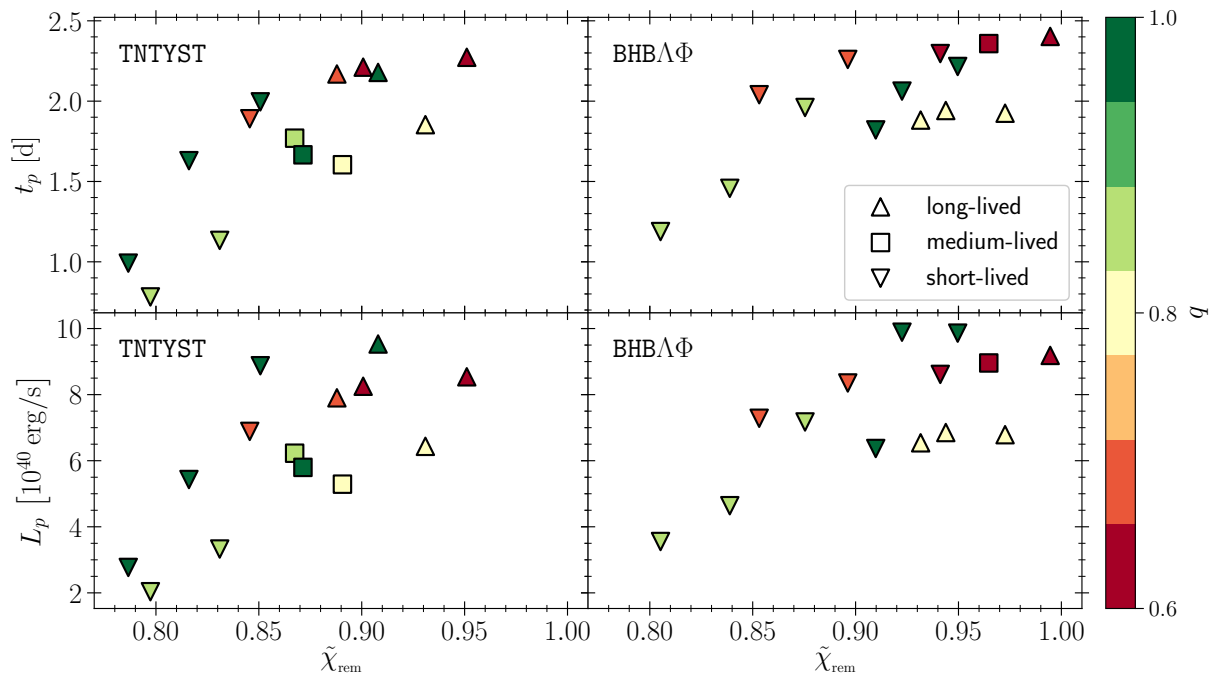


**Figure 8.** *Left panel:* Behaviour of the characteristic properties of the kilonova emission, i.e., the time of peak emission (top part) and the luminosity at peak (lower part) for binaries modeled with the TNTYST EOS and shown as a function of the total dimensionless spin at merger of the remnant. Different symbols follow the convention presented in Tab. 1 and refer to the different lifetime of the remnants. Shown with a colourcode is the corresponding mass ratio in the binary. *Right panel:* the same as the left panel but for the BHB $\Lambda\Phi$  EOSs.

resulting from equal-mass systems. At the same time, the dependence of the remnant lifetime on the mass ratio can either be monotonic, as in the case of the softer TNTYST, or show a local maximum for intermediate mass ratios, e.g.,  $q = 0.8$  for the stiffer BHB $\Lambda\Phi$  EOS.

- The remnant-disc masses, and therefore also the secular ejecta, can vary significantly and up to three orders of magnitude in the space of parameters considered. In particular, the largest disc masses are produced by binaries with large primary spin and small mass ratio; by contrast, the smallest disc masses are produced by binaries with small primary spin and equal masses.

- Also the dynamically ejected matter can vary significantly across our simulated binaries. More specifically, large (small) amounts of ejected mass are again found for binaries with large (small) primary spin and small (large) mass ratios. However, the largest amounts of dynamical ejecta has been found for binaries with very large primary spin but equal masses.

- A nonlinear correlation is present between the peak properties of the kilonova emission and the dimensionless spin of the remnant at merger. In particular, large spins will systematically lead to peak times  $t_p$  delayed of up to one day and to luminosities  $L_p$  that are up to a factor five larger. While these delays and increased luminosities can be interpreted as due to highly spinning binaries or small mass ratios, a more accurate modelling of the kilonova emission is needed.

Overall, the results obtained show that the merger of BNSs with small mass ratios and rapidly spinning primaries offer exciting prospects for the detection of an electromagnetic counterpart as they systematically increase the lifetime of the remnant and boost the ejected mass, either dynamically or via a secular emission from the disc. It is presently unclear whether systems with these properties occur in nature, just as it is difficult from the inspiral signal alone to determine with precision what is the mass ratio and the spins of

the components. This study thus highlights that a number of hints on binaries with extreme spins and mass ratios can be found in their electromagnetic counterparts, which we will model in future work.

## ACKNOWLEDGEMENTS

The authors gratefully acknowledge funding by the State of Hesse within the Research Cluster ELEMENTS (Project ID 500/10.006), by the ERC Advanced Grant “JETSET: Launching, propagation and emission of relativistic jets from binary mergers and across mass scales” (Grant No. 884631), and by HGS-HIRE for FAIR. ERM acknowledges support from a joint fellowship at the Princeton Center for Theoretical Science, the Princeton Gravity Initiative and the Institute for Advanced Study. Part of the simulations were performed on the national supercomputer HPE Apollo Hawk at the High Performance Computing Center Stuttgart (HLRS) under allocations BB-HDISKS and BNSMIC, and the GCS Supercomputer SuperMUC at Leibniz Supercomputing Centre (www.lrz.de) This work benefited from the valuable implementations in the *kuibit* (Bozzola 2021), *SciPy* (Virtanen et al. 2020), *NumPy* (Harris et al. 2020) and *matplotlib* (Hunter 2007) libraries.

## DATA AVAILABILITY

Data is available upon reasonable request from the Corresponding Author.

## REFERENCES

Abbott B. P., et al., 2018, *Physical Review Letters*, **121**, 161101

- Abbott B. P., et al., 2019, *Physical Review X*, 9, 011001
- Abbott B. P., et al., 2020, *Astrophys. J. Lett.*, 892, L3
- Agathos M., Meidam J., Del Pozzo W., Li T. G. F., Tompitak M., Veitch J., Vitale S., Van Den Broeck C., 2015, *Phys. Rev. D*, 92, 023012
- Agathos M., Zappa F., Bernuzzi S., Perego A., Breschi M., Radice D., 2020, *Phys. Rev. D*, 101, 044006
- Alic D., Bona-Casas C., Bona C., Rezzolla L., Palenzuela C., 2012, *Phys. Rev. D*, 85, 064040
- Alsing J., Silva H. O., Berti E., 2018, *Mon. Not. R. Astron. Soc.*, 478, 1377
- Andrews J. J., Mandel I., 2019, *Astrophys. J. Lett.*, 880, L8
- Annala E., Gorda T., Kurkela A., Vuorinen A., 2018, *Phys. Rev. Lett.*, 120, 172703
- Antoniadis J., Freire P. C. C., Wex N., Tauris T. M., Lynch R. S., et al. 2013, *Science*, 340, 448
- Arzoumanian Z., et al., 2018, *Astrophys. J., Suppl.*, 235, 37
- Baiotti L., Rezzolla L., 2017, *Rept. Prog. Phys.*, 80, 096901
- Baiotti L., Giacomazzo B., Rezzolla L., 2008, *Phys. Rev. D*, 78, 084033
- Banik S., Hempel M., Bandyopadhyay D., 2014, *Astrophys. J. Suppl.*, 214, 22
- Bauswein A., Janka H.-T., 2012, *Phys. Rev. Lett.*, 108, 011101
- Bauswein A., Baumgarte T. W., Janka H.-T., 2013, *Phys. Rev. Lett.*, 111, 131101
- Bauswein A., Just O., Janka H.-T., Stergioulas N., 2017, *Astrophys. J. Lett.*, 850, L34
- Bauswein A., et al., 2020, arXiv e-prints, p. arXiv:2004.00846
- Bauswein A., Blacker S., Lioutas G., Soultanis T., Vijayan V., Stergioulas N., 2021, *Phys. Rev. D*, 103, 123004
- Benacquista M. J., Downing J. M. B., 2013, *Living Reviews in Relativity*, 16, 4
- Bernuzzi S., Hilditch D., 2010, *Phys. Rev. D*, 81, 084003
- Bernuzzi S., Dietrich T., Tichy W., Brügmann B., 2014, *Phys. Rev. D*, 89, 104021
- Bernuzzi S., Dietrich T., Nagar A., 2015, *Phys. Rev. Lett.*, 115, 091101
- Bernuzzi S., et al., 2020, arXiv e-prints, p. arXiv:2003.06015
- Bishop N. T., Rezzolla L., 2016, *Living Reviews in Relativity*, 19, 2
- Bona C., Ledvinka T., Palenzuela C., Záček M., 2003, *Phys. Rev. D*, 67, 104005
- Bovard L., Rezzolla L., 2017, *Classical and Quantum Gravity*, 34, 215005
- Bovard L., Martin D., Guercilena F., Arcones A., Rezzolla L., Korobkin O., 2017, *Phys. Rev. D*, 96, 124005
- Bozzola G., 2021, *The Journal of Open Source Software*, 6, 3099
- Breu C., Rezzolla L., 2016, *Mon. Not. R. Astron. Soc.*, 459, 646
- Burderi L., Possenti A., Colpi M., Di Salvo T., D'Amico N., 1999, *Astrophys. J.*, 519, 285
- Christie I. M., Lalakos A., Tchekhovskoy A., Fernández R., Foucart F., Quataert E., Kasen D., 2019, *Mon. Not. R. Astron. Soc.*, 490, 4811
- Cromartie H. T., et al., 2020, *Nature Astronomy*, 4, 72
- Cruz-Osorio A., Rezzolla L., 2020, *Astrophys. J.*, 894, 147
- De S., Finstad D., Lattimer J. M., Brown D. A., Berger E., Biwer C. M., 2018, *Physical Review Letters*, 121, 091102
- Del Zanna L., Zanotti O., Bucciantini N., Londrillo P., 2007, *Astron. Astrophys.*, 473, 11
- Demorest P. B., Pennucci T., Ransom S. M., Roberts M. S. E., Hessels J. W. T., 2010, *Nature*, 467, 1081
- Dietrich T., Moldenhauer N., Johnson-McDaniel N. K., Bernuzzi S., Markakis C. M., Brügmann B., Tichy W., 2015, *Phys. Rev. D*, 92, 124007
- Dietrich T., Ujevic M., Tichy W., Bernuzzi S., Brügmann B., 2017a, *Phys. Rev. D*, 95, 024029
- Dietrich T., Bernuzzi S., Ujevic M., Tichy W., 2017b, *Phys. Rev. D*, 95, 044045
- Dominik M., Belczynski K., Fryer C., Holz D. E., Berti E., Bulik T., Mandel I., O'Shaughnessy R., 2013, *Astrophys. J.*, 779, 72
- East W. E., Paschalidis V., Pretorius F., 2016a, *Classical and Quantum Gravity*, 33, 244004
- East W. E., Paschalidis V., Pretorius F., Shapiro S. L., 2016b, *Phys. Rev. D*, 93, 024011
- East W. E., Paschalidis V., Pretorius F., Tsokaros A., 2019, *Phys. Rev. D*, 100, 124042
- Etienne Z. B., Paschalidis V., Haas R., Mösta P., Shapiro S. L., 2015, *Class. Quantum Grav.*, 32, 175009
- Even W., et al., 2020, *Astrophys. J.*, 899, 24
- Favata M., 2014, *Phys. Rev. Lett.*, 112, 101101
- Fernández R., Tchekhovskoy A., Quataert E., Foucart F., Kasen D., 2019, *Mon. Not. R. Astron. Soc.*, 482, 3373
- Fonseca E., et al., 2016, *Astrophys. J.*, 832, 167
- Foucart F., et al., 2016, *Phys. Rev. D*, 93, 044019
- Fujibayashi S., Sekiguchi Y., Kiuchi K., Shibata M., 2017, *Astrophys. J.*, 846, 114
- Fujibayashi S., Kiuchi K., Nishimura N., Sekiguchi Y., Shibata M., 2018, *The Astrophysical Journal*, 860, 64
- Galeazzi F., Kastaun W., Rezzolla L., Font J. A., 2013, *Phys. Rev. D*, 88, 064009
- Gill R., Nathanael A., Rezzolla L., 2019, *Astrophys. J.*, 876, 139
- Grandclement P., 2010, *J. Comput. Phys.*, 229, 3334
- Grossman D., Korobkin O., Rosswog S., Piran T., 2014, *Mon. Not. R. Astron. Soc.*, 439, 757
- Hanauske M., Takami K., Bovard L., Rezzolla L., Font J. A., Galeazzi F., Stöcker H., 2017, *Phys. Rev. D*, 96, 043004
- Hannam M., Schmidt P., Bohé A., Haegel L., Husa S., Ohme F., Pratten G., Pürrer M., 2014, *Phys. Rev. Lett.*, 113, 151101
- Harris C. R., et al., 2020, *Nature*, 585, 357
- Harry I., Hinderer T., 2018, *Classical and Quantum Gravity*, 35, 145010
- Hempel M., Schaffner-Bielich J., 2010, *Nuclear Physics A*, 837, 210
- Hessels J. W., Ransom S. M., Stairs I. H., Freire P. C., Kaspi V. M., Camillo F., 2006, *Science*, 311, 1901
- Hunter J. D., 2007, *Computing In Science & Engineering*, 9, 90
- Israel G. L., et al., 2017, *Science*, 355, 817
- Kastaun W., Galeazzi F., Alic D., Rezzolla L., Font J. A., 2013, *Phys. Rev. D*, 88, 021501
- Kawaguchi K., Shibata M., Tanaka M., 2018, *Astrophys. J. Lett.*, 865, L21
- Koeppel S., Bovard L., Rezzolla L., 2019, *Astrophys. J. Lett.*, 872, L16
- Kölsch M., Dietrich T., Ujevic M., Bruegmann B., 2021, arXiv e-prints, p. arXiv:2112.11851
- Korobkin O., et al., 2021, *Astrophys. J.*, 910, 116
- Kruckow M. U., Tauris T. M., Langer N., Kramer M., Izzard R. G., 2018, *Mon. Not. R. Astron. Soc.*, 481, 1908
- Lazarus P., et al., 2016, *Astrophys. J.*, 831, 150
- Lehner L., Liebling S. L., Palenzuela C., Caballero O. L., O'Connor E., Anderson M., Neilsen D., 2016a, *Classical and Quantum Gravity*, 33, 184002
- Lehner L., Liebling S. L., Palenzuela C., Motl P. M., 2016b, *Phys. Rev. D*, 94, 043003
- Loeffler F., et al., 2012, *Class. Quantum Grav.*, 29, 115001
- Lorimer D. R., 2008, *Living Rev. Relativ.*, 8
- Lynch R. S., Freire P. C. C., Ransom S. M., Jacoby B. A., 2012, *Astrophys. J.*, 745, 109
- Lyne A. G., et al., 2004, *Science*, 303, 1153
- MacLeod M., Ramirez-Ruiz E., 2015, *Astrophys. J. Lett.*, 798, L19
- Malik T., Alam N., Fortin M., Providência C., Agrawal B. K., Jha T. K., Kumar B., Patra S. K., 2018, *Physical Review C*, 98, 035804
- Manca G. M., Baiotti L., DePietri R., Rezzolla L., 2007, *Class. Quantum Grav.*, 24, S171
- Manchester R. N., Hobbs G. B., Teoh A., Hobbs M., 2005, *Astronomical Journal*, 129, 1993
- Margalit B., Metzger B. D., 2017, *Astrophys. J. Lett.*, 850, L19
- Martinez J. G., et al., 2015, *Astrophys. J.*, 812, 143
- Metzger B. D., 2017, *Living Reviews in Relativity*, 20, 3
- Metzger B. D., Fernández R., 2014, *Mon. Not. R. Astron. Soc.*, 441, 3444
- Miller M. C., Miller J. M., 2015, *Phys. Rep.*, 548, 1
- Montaña G., Tolós L., Hanauske M., Rezzolla L., 2019, *Phys. Rev. D*, 99, 103009
- Most E. R., Raithel C. A., 2021, arXiv e-prints, p. arXiv:2107.06804
- Most E. R., Weih L. R., Rezzolla L., Schaffner-Bielich J., 2018, *Phys. Rev. Lett.*, 120, 261103
- Most E. R., Papenfort L. J., Dexheimer V., Hanauske M., Schramm S., Stöcker H., Rezzolla L., 2019a, *Physical Review Letters*, 122, 061101

- Most E. R., Papenfort L. J., Rezzolla L., 2019b, *Mon. Not. R. Astron. Soc.*, **490**, 3588
- Most E. R., Papenfort L. J., Tsokaros A., Rezzolla L., 2019c, *Astrophys. J.*, **884**, 40
- Most E. R., Weih L. R., Rezzolla L., 2020a, *Mon. Not. R. Astron. Soc.*, **496**, L16
- Most E. R., Papenfort L. J., Weih L. R., Rezzolla L., 2020b, *Mon. Not. R. Astron. Soc.*, **499**, L82
- Most E. R., Papenfort L. J., Tootle S. D., Rezzolla L., 2021, *Astrophys. J.*, **912**, 80
- Murguía-Berthier A., MacLeod M., Ramirez-Ruiz E., Antoni A., Macias P., 2017, *Astrophys. J.*, **845**, 173
- Nathanail A., Most E. R., Rezzolla L., 2021, *Astrophys. J. Lett*, in press, p. [arXiv:2101.01735](https://arxiv.org/abs/2101.01735)
- Nedora V., Bernuzzi S., Radice D., Perego A., Endrizzi A., Ortiz N., 2019, *Astrophys. J. Lett.*, **886**, L30
- Neilsen D. W., Liebling S. L., Anderson M., Lehner L., O'Connor E., Palenzuela C., 2014, *Phys. Rev. D*, **89**, 104029
- Palenzuela C., Liebling S. L., Neilsen D., Lehner L., Caballero O. L., O'Connor E., Anderson M., 2015, *Phys. Rev. D*, **92**, 044045
- Papenfort L. J., Gold R., Rezzolla L., 2018, *Phys. Rev. D*, **98**, 104028
- Papenfort L. J., Tootle S., Grandclement P., Most E. R., Rezzolla L., 2020, in preparation
- Paschalidis V., East W. E., Pretorius F., Shapiro S. L., 2015, *Phys. Rev. D*, **92**, 121502
- Perego A., Rosswog S., Cabezon R. M., Korobkin O., Käppeli R., Arcones A., Liebendörfer M., 2014, *Mon. Not. R. Astron. Soc.*, **443**, 3134
- Perego A., Logoteta D., Radice D., Bernuzzi S., Kashyap R., Das A., Padamata S., Prakash A., 2021, arXiv e-prints, p. [arXiv:2112.05864](https://arxiv.org/abs/2112.05864)
- Pfeiffer H. P., York J. W., 2003, *Phys. Rev. D*, **67**, 044022
- Pfeiffer H. P., York J. W., 2005, *Phys. Rev. Lett.*, **95**, 091101
- Radice D., Bernuzzi S., Ott C. D., 2016a, *Phys. Rev. D*, **94**, 064011
- Radice D., Galeazzi F., Lippuner J., Roberts L. F., Ott C. D., Rezzolla L., 2016b, *Mon. Not. R. Astron. Soc.*, **460**, 3255
- Radice D., Perego A., Zappa F., Bernuzzi S., 2018a, *Astrophys. J. Lett.*, **852**, L29
- Radice D., Perego A., Hotokezaka K., Fromm S. A., Bernuzzi S., Roberts L. F., 2018b, *Astrophys. J.*, **869**, 130
- Raithel C., Özel F., Psaltis D., 2018, *Astrophys. J.*, **857**, L23
- Rawls M. L., Orosz J. A., McClintock J. E., Torres M. A. P., Bailyn C. D., Buxton M. M., 2011, *Astrophys. J.*, **730**, 25
- Rezzolla L., Takami K., 2016, *Phys. Rev. D*, **93**, 124051
- Rezzolla L., Baiotti L., Giacomazzo B., Link D., Font J. A., 2010, *Class. Quantum Grav.*, **27**, 114105
- Rezzolla L., Most E. R., Weih L. R., 2018, *Astrophys. J. Lett.*, **852**, L25
- Ridolfi A., et al., 2021, *MNRAS*, **504**, 1407
- Rosswog S., Liebendörfer M., 2003, *Mon. Not. R. Astron. Soc.*, **342**, 673
- Ruffert M., Janka H.-T., Schaefer G., 1996, *Astron. Astrophys.*, **311**, 532
- Ruiz M., Shapiro S. L., Tsokaros A., 2018, *Phys. Rev. D*, **97**, 021501
- Savitzky A., Golay M. J. E., 1964, *Analytical Chemistry*, **36**, 1627
- Schnetter E., Hawley S. H., Hawke I., 2004, *Class. Quantum Grav.*, **21**, 1465
- Shibata M., Taniguchi K., 2006, *Phys. Rev. D*, **73**, 064027
- Shibata M., Taniguchi K., Uryū K., 2003, *Phys. Rev. D*, **68**, 084020
- Shibata M., Taniguchi K., Uryū K., 2005, *Phys. Rev. D*, **71**, 084021
- Shibata M., Zhou E., Kiuchi K., Fujibayashi S., 2019, *Phys. Rev. D*, **100**, 023015
- Siegel D. M., Metzger B. D., 2017, *Physical Review Letters*, **119**, 231102
- Siegel D. M., Metzger B. D., 2018, *Astrophys. J.*, **858**, 52
- Stovall K., et al., 2018, *Astrophys. J. Letters*, **854**, L22
- Tacik N., et al., 2015, *Phys. Rev. D*, **92**, 124012
- Takami K., Rezzolla L., Baiotti L., 2014, *Phys. Rev. Lett.*, **113**, 091104
- Tanaka M., et al., 2018, *Astrophys. J.*, **852**, 109
- Tauris T. M., Janka H.-T., 2019, *Astrophys. J. Lett.*, **886**, L20
- Tauris T. M., Langer N., Kramer M., 2012, *Mon. Not. R. Astron. Soc.*, **425**, 1601
- Tauris T. M., Langer N., Podsiadlowski P., 2015, *Mon. Not. R. Astron. Soc.*, **451**, 2123
- Tauris T. M., et al., 2017, *Astrophys. J.*, **846**, 170
- Tews I., Margueron J., Reddy S., 2018, *Physical Review C*, **98**, 045804
- The LIGO Scientific Collaboration The Virgo Collaboration 2017, *Phys. Rev. Lett.*, **119**, 161101
- The LIGO Scientific Collaboration et al., 2020, *Astrophys. J. Lett.*, **896**, L44
- Tichy W., 2012, *Phys. Rev. D*, **86**, 064024
- Tichy W., Rashti A., Dietrich T., Dudi R., Brüggemann B., 2019, *Phys. Rev. D*, **100**, 124046
- Togashi H., Nakazato K., Takehara Y., Yamamuro S., Suzuki H., Takano M., 2017, *Nucl. Phys.*, **A961**, 78
- Tootle S. D., Papenfort L. J., Most E. R., Rezzolla L., 2021, arXiv e-prints, p. [arXiv:2109.00940](https://arxiv.org/abs/2109.00940)
- Tsokaros A., Uryū K., Rezzolla L., 2015, *Phys. Rev. D*, **91**, 104030
- Tsokaros A., Mundim B. C., Galeazzi F., Rezzolla L., Uryū K., 2016, *Phys. Rev. D*, **94**, 044049
- Virtanen P., et al., 2020, *Nature Methods*, **17**, 261
- Wollaeger R. T., et al., 2018, *Mon. Not. R. Astron. Soc.*, **478**, 3298
- Wollaeger R. T., et al., 2021, arXiv e-prints, p. [arXiv:2105.11543](https://arxiv.org/abs/2105.11543)
- Zhu X., Thrane E., Osłowski S., Levin Y., Lasky P. D., 2018, *Phys. Rev. D*, **98**, 043002

## APPENDIX A: MEASURING THE UNCERTAINTY IN OUR ESTIMATES

With the goal of measuring the uncertainty in the various quantities presented in this paper, we have repeated our analysis for all of the models at the lower resolution of  $h = 0.2M_{\odot}$  and thus a factor in volume resolution of  $\sim 2$ . We have also carried out four simulations at a higher resolution of  $h = 0.133M_{\odot}$ , which are obviously considerably more expensive. These models are selected to be at the high-mass end of the configurations, three with the TTYST EOS and different mass ratios and spins, as well as one binary with the BHB $\Lambda\Phi$  EOS. While this analysis does not allow us to conduct a detailed convergence analysis, it gives us an estimate and approximate upper bound on the resolution-dependent uncertainties. These uncertainties have been collected in four distinct classes depending on the quantity considered. They are: a) inspiral and post-merger GW radiation; b) post-merger survival time of the HMNS; c) dynamical ejecta; d) disc mass and thus the approximate total ejected mass on secular time-scales. All of these uncertainties are discussed in detail below. In summary, our uncertainties are of few tens of percent at most; in this sense, they are comparable or smaller than those reported by other groups in similar investigations (Radice et al. 2018b; Nedora et al. 2019).

a) To assess the discretization-dependent uncertainties in the post-merger GW radiation, i.e., including the cumulative effect of the quantities presented in Fig. 4, we calculated the relative differences between both resolutions for both the total radiated angular momentum and the radiated energy. In all cases and quantities the average absolute relative difference is 12% (median 11%), including a few showing differences of up to  $\leq 50\%$ , while no correlation with the absolute magnitude of the particular quantity is detectable. Additionally, the cumulative post-merger radiation is on average smaller at lower resolution for both quantities and modes. The inspiral GW emission is completely dominated by the (2, 2) emission leading to an overall average uncertainty of at most 2% for both quantities. Comparing to the high-resolution (low), the maximum relative differences in the post-merger radiation is  $\approx 10\%$  ( $\approx 21\%$ ), while the averages decrease to  $\leq 4\%$  ( $\leq 6\%$ ) for the post-merger and 1% (2%) for the inspiral emission.

b) In the case of the post-merger survival time of the HMNS, most of the short lifetimes are well below the low-resolution sampling rate, while one of these models reaches a relative difference in the

survival time of 50%. At larger survival times, the same reach a difference of 30%. Overall, discretization-dependent uncertainty in the estimate of the lifetime is of  $\lesssim 8\%$  (median  $\lesssim 3\%$ ). A correlation with increasing survival times is expected, but due to the sparsity of intermediate lifetimes, this could not be verified. Nonetheless, the survival times are on average smaller at lower resolution. For the high-resolution (low-) sample, with three collapsing models, the relative difference in the lifetime estimate is  $\simeq 1\%$  (3%). It should be noted though that, due to the high costs of these simulations, we do not include models with intermediate or longer lifetimes (the lifetime is 1.17 ms at most within this sample), so that significantly larger relative differences can develop over longer lifetimes also at these rather high resolution.

c) For the dynamical ejecta we employed two different uncertainty estimates. First, again, the differences between the total ejected mass is compared between different resolutions. In addition to the standard-resolution result, we also compute the relative differences with respect to the extrapolated total ejected mass  $M_{\text{tot}}$ . The binaries with the smallest dynamically ejected mass show the largest deviations between the two resolutions, reaching  $\lesssim 150\%$ . This is because of the very low densities reached in these cases that can be masked into the atmosphere in the low-resolutions outer regions of the simulation domain. Note that these differences are nonetheless insignificant when considering the total mass ejected, whose relative difference is still well below 0.1%. Overall, the average absolute relative differences in the measurement of the dynamically ejected mass is 26% (median 20%). We have also explored how our estimates change with the placement of the outer detectors. In particular, we have recomputed the dynamically ejected masses at a distance of 443 km from the merger remnant and compared the result with those measured at 295 km. In this case, we see a weak correlation with the total ejected mass, where the differences peak at 28% together with an average of 7% (median 3%). The observed correlation confirms the validity of our choice in a detector that is closer to the merger remnant. This is because the resolution drops outwards in the simulation domain – due to the box-in-box mesh refinement – so that the mass estimates are less accurate especially when lower densities towards atmosphere levels are involved. The high-resolution sample of models includes the two cases with strongly suppressed dynamical ejecta leading to large uncertainties of 100% and 163%, respectively. This indicates that the resolution in the outer regions of the grid is still too coarse to draw conclusions that are accurate beyond an order of magnitude estimate. When considering the whole sample of high-resolution (low-) binaries, the average relative uncertainty decreases to 65% (80%). This is because the other two binaries have far smaller relative uncertainties of 1% (5 – 20%).

d) Important for the electromagnetic follow-up emission are the uncertainties in the disc mass and thus the mass fraction ejected on secular timescales [see Eq. (2)]. As in the case of the dynamical ejecta, we examined two independent sources of uncertainty. Due to lack of full three-dimensional datasets needed to measure the discs around the HMNS, we limit our analysis to the models collapsing within the simulation time. For these cases, the discretization-dependent uncertainty estimate reaches a maximum value of 76%, but the deviation is much smaller for the most massive discs, while the average is  $\approx 10\%$  (median 3%). Within the high resolution sample we included the largest deviating model mentioned above. The outlier drops from 76% to mere 1% indicating that the low-resolution simulation is not able to capture the full dynamics involving the creation of the disc accurately. At the same time, also the other uncertainties decrease leading to an average and median of the high-resolution (low-) sample of both 2% (average 28%, median 7%). In summary,

the discretization error on the extrapolated total ejected mass  $M_{\text{tot}}$  is most probably dominated by the disc-mass estimates, except for the models with the largest dynamical ejecta.

A second source of error, which inevitably leads to an overestimation of the disc mass, is that it is not possible to reach a perfectly stationary disc over the timescales simulated. Since the disc mass measurements reach quasi-constant values on exponential timescales, we model the future accreted matter by an exponentially decaying contribution to the disc mass estimate. This is underpinned by the fact that the post-collapse tail of the accretion rate, i.e., the time derivative of the disc mass estimate, is observed to be log-linear Rezzolla et al. (2010). Fitting this tail gives us an estimate on the yet to be accreted mass for  $t \rightarrow \infty$ . The maximal value reaches 36%, with an average of 14% (median 13%). While these represent a significant systematic effect with respect to the true post-collapse disc mass, we do not correct for them here. We note that the evolution and subsequent effect of magnetic fields and neutrino absorption are important for the equilibration of the disc, which are not included in our simple estimates of the long-term accretion.

This paper has been typeset from a  $\text{\TeX}/\text{\LaTeX}$  file prepared by the author.